

Positron annihilation spectrum from the Galactic Centre region observed by *SPI/INTEGRAL* revisited: annihilation in a cooling ISM?

E. Churazov,^{1,2*} S. Sazonov,² S. Tsygankov,^{1,2} R. Sunyaev^{1,2} and D. Varshalovich³

¹Max-Planck-Institut für Astrophysik, Karl-Schwarzschild-Strasse 1, 85741 Garching, Germany

²Space Research Institute (IKI), Profsoyuznaya 84/32, Moscow 117997, Russia

³Ioffe Physical Technical Institute, Polytekhnicheskaya 26, St Petersburg 194021, Russia

Accepted 2010 October 1. Received 2010 September 26; in original form 2009 December 31

ABSTRACT

We analyse *SPI/INTEGRAL* data on the 511-keV line from the Galactic Centre, accumulated over ~ 6 yr of observations. We decompose the X-ray and soft gamma-ray emission of the central part of the Milky Way into relatively compact ‘bulge’ and more extended ‘disc’ components and report their spectral properties. The bulge component shows a prominent 511-keV line and essentially no flux at 1.8 MeV, while the disc component on the contrary contains a prominent 1.8-MeV line and a very weak annihilation line.

We show that the spectral shape of the annihilation radiation (the narrow 511-keV line and the associated ortho-positronium continuum) is surprisingly well described by a model of annihilation of hot positrons in a radiatively cooling interstellar medium (ISM). The model assumes that positrons are initially injected into a hot ($\sim 10^6$ K), volume-filling ISM, which is allowed to freely cool via radiative losses. The annihilation time in such a medium is longer than the cooling time for temperatures higher than a few 10^4 K. Thus, most of the positrons annihilate only after the gas has cooled down to $\sim 10^5$ K, giving rise to annihilation emission characteristic of a warm, ionized ISM.

Key words: ISM: general – Galaxy: centre – gamma-rays: ISM.

1 INTRODUCTION

Although the annihilation line of positrons at 511 keV is the brightest gamma-ray line in the Galaxy, the origin of the annihilating positrons is not yet firmly established. First observed with an NaI scintillator as an ~ 476 -keV line coming from the Galactic Centre (GC) region (Johnson, Harnden & Haymes 1972; Johnson & Haymes 1973), it was subsequently unambiguously identified with a narrow [full width at half-maximum (FWHM) of < 3.2 keV] e^+e^- annihilation line using germanium detectors (Leventhal, MacCallum & Stang 1978). Since then, many balloon flights and several space missions (e.g. Gehrels et al. 1991; Mahoney, Ling & Wheaton 1994; Teegarden et al. 1996; Purcell et al. 1997) have measured the spatial distribution and spectral properties of the line.

Since 2003, *INTEGRAL* data on the 511-keV line emission have become available. These data show that there is a strong, $\sim 10^{-3}$ photon $s^{-1} cm^{-2}$, source of 511-keV photons at the centre of the Milky Way with an FWHM of 6° – 8° (e.g. Jean et al. 2003; Churazov et al. 2005; Knödlseder et al. 2005), while the 511-keV flux coming from the Galactic plane is much less constrained by the *INTEGRAL* data (e.g. Teegarden et al. 2005; Bouchet et al. 2008).

No significant variability in the narrow 511-keV line has been found in the *SPI* data (Tsygankov & Churazov 2010). The spectrum of the annihilation radiation from the GC region observed by *SPI* can be reasonably well described as a combination of a narrow line (~ 2 – 3 keV Gaussian at 511 keV) and a three-photon continuum. The flux ratio of the three-photon continuum to the narrow line suggests that the majority of positrons form positronium prior to annihilation (e.g. Churazov et al. 2005; Jean et al. 2006).

In spite of numerous observations, the origin of the 511-keV emission from the GC is not established. The problem can be summarized as follows.

(1) The morphology of the observed 511-keV line emission does not fit the disc-like spatial distribution of such obvious sources of positrons as (i) massive stars, which produce β^+ unstable nuclei-like ^{26}Al , or (ii) π^+ s generated by the interaction of cosmic rays with the interstellar medium (ISM). This favours scenarios with a more prominent central excess (‘bulge dominated’), including the old stellar population [e.g. supernovae Ia (SNIa)], activity of Sgr A* and the annihilation of dark matter particles.

(2) The spectrum of the annihilation emission (narrow linewidth and the flux ratio of the line to three-photon continuum) suggests that positrons are annihilating in a warm, $\sim 10^4$ K, and slightly ionized, approximately a few per cent, medium (e.g. Churazov et al. 2005; Jean et al. 2006). Such an ISM phase does exist in the Galaxy, but

*E-mail: churazov@mpa-garching.mpg.de

its spatial distribution is strongly concentrated towards the plane, posing the problem of ‘finding’ the right ISM phase by a positron.

Recently, an attempt to build a self-consistent picture was presented by Higdon, Lingenfelter & Rothschild (2009) and Lingenfelter, Higdon & Rothschild (2009), who assumed that the spatial propagation of positrons, produced via β^+ decay of ^{56}Ni , ^{44}Ti and ^{26}Al , is governed by a diffusion process with the effective diffusion coefficient different in the bulge and the disc of the Galaxy. During diffusion the positrons enter the H II and H I envelopes of molecular clouds, in particular those forming a ‘tilted disc’ (Ferrière, Gillard & Jean 2007) within 1.5 kpc of the GC. The model of Higdon et al. (2009), with a reasonable set of assumptions, can explain the basic properties of the annihilation radiation.

Here we take an alternative route and consider a possibility that a significant fraction of positrons are born in the hot ISM, which is eventually able to cool via radiative losses and perhaps via adiabatic expansion. We show below that with these assumptions, the spectral properties of the 511-keV line can be easily explained. However, to make our picture self-consistent one needs to model the thermal state of the ISM, which is beyond the scope of this paper.

This paper is based on the *INTEGRAL* data accumulated over ~ 6 yr of observations and aims at placing tighter constraints on the spectral and spatial properties of the annihilation emission.

2 DATA AND BACKGROUND HANDLING

SPI is a coded mask germanium spectrometer on board *INTEGRAL* (Winkler et al. 2003), launched in 2002 October aboard a PROTON rocket. The instrument consists of 19 individual Ge detectors, has a field of view (FOV) of $\sim 30^\circ$ (at zero response), an effective area at 511 keV of $\sim 70 \text{ cm}^2$ and an energy resolution of $\sim 2 \text{ keV}$ (Vedrenne et al. 2003). The good energy resolution makes SPI an appropriate instrument for studying the spectrum of e^+e^- annihilation emission.

For our analysis we use all data that were available to us by mid-2009, including public data and some proprietary data (in particular, proposals 0420073, 0520071 and parts of 0620059). Prior to actual data analysis, all individual observations were screened for periods of a very high particle background. We use the SPI anticoincidence shield (ACS) shield rate as the main indicator of a high background. Several additional observations were also omitted from the analysis, e.g. those taken shortly after SPI annealing procedures (Roques et al. 2003). For our analysis, we used a combination of single and pulse-shape-discriminator events (see Roques et al. 2003, for details) and treated them in the same way.

2.1 Energy gain and resolution

For each detector, a linear relation between the energy and the channel number was assumed and calibrated (separately for each orbit), using the observed energies of lines at $\sim 198, 438, 584, 882, 1764, 1779, 2223$ and 2754 keV [see Weidenspointner et al. (2003) for a comprehensive list of SPI background lines]. With this calibration, the rms deviation of the background 511-keV line energy (revolution based) is 0.0066 keV while the mean energy of the line is 510.926 keV . There is thus a small deviation of the line mean energy from the electron rest energy (510.999 keV): $\Delta E = 0.07 \text{ keV}$; it can be attributed to the simplified linear energy/channel relation. This deviation is comparable to the statistical uncertainty on the line energy (see Section 5), and no attempt was made to correct for this effect.

Since the background 511-keV line (produced by the positrons annihilating in the body of the detector) is kinematically broadened, we used the two bracketing lines (at 438 and 584 keV) to calculate the resolution at 511 keV as $\text{FWHM}_{511} = 0.5 \times (\text{FWHM}_{438} + \text{FWHM}_{584})$. The resulting value is $\text{FWHM}_{511} = 2.175 \text{ keV}$ when averaged over all observations in the vicinity of the GC.

2.2 Background modelling

In the background modelling, we followed the scheme used in Churazov et al. (2005). Namely, the background count rate $B(i, E)$ in detector i at energy E is assumed to be proportional to the detector-saturated (i.e. above 8 MeV) event rate R_{sat} and time t :

$$B(i, E) = C(i, E) + \alpha(i, E)R_{\text{sat}} + \beta(i, E)t, \quad (1)$$

where $i = 1, 19$ is the detector number. The coefficients $\alpha(i, E)$ and $\beta(i, E)$ of this linear relation were determined separately for each detector/energy channel using all the available SPI data, while the constant $C(i, E)$ was estimated using only the data away from the Galactic plane and away from bright sources. The whole data set was divided into 14 time intervals (defined by the annealing periods and the dates of individual detector failures¹), and the coefficients $\alpha(i, E)$, $\beta(i, E)$ and $C(i, E)$ were determined separately for each interval. This procedure, although not providing a perfect description of the background, works reasonably well at all energies and, given the small number of free parameters, is very robust. For instance, the relative rms deviation of the 600–1000 keV flux (averaged over one revolution) from the count rate predicted by this model is $\sim 1.3 \times 10^{-3}$.

Along with our reference background model, we made several experiments by dividing the full data set into different time intervals and modifying the selection criteria used for cleaning the data from background flares. In these experiments, we generated several ‘alternative’ background models. Below, we use these models to test the sensitivity of our results to the details of the background modelling.

3 IMAGING

Imaging with coded mask telescopes often requires additional assumptions to be made on the sky surface brightness distribution, e.g. sparsity of compact sources or regular behaviour of diffuse emission. This is especially important for the SPI telescope, which has only $n = 19$ independent detectors/pixels. This makes image reconstruction in a single observation problematic, given that a typical image reconstruction procedure relies on the smallness of the parameter $1/n$ with respect to unity. We have chosen not to make a priori assumptions about the spatial distribution of sources and restricted ourselves to three different types of ‘imaging’: (i) light-bucket imaging, (ii) simple parametric models and (iii) linear decomposition of the sky surface brightness into few simple templates.

3.1 Light-bucket mapping

In this simple ‘imaging’ procedure, for each observation, the background-subtracted counts in a given energy band are summed over all detectors and the resulting signal is added to the pixel of

¹ Three out of the 19 SPI detectors had failed by the end of 2009.

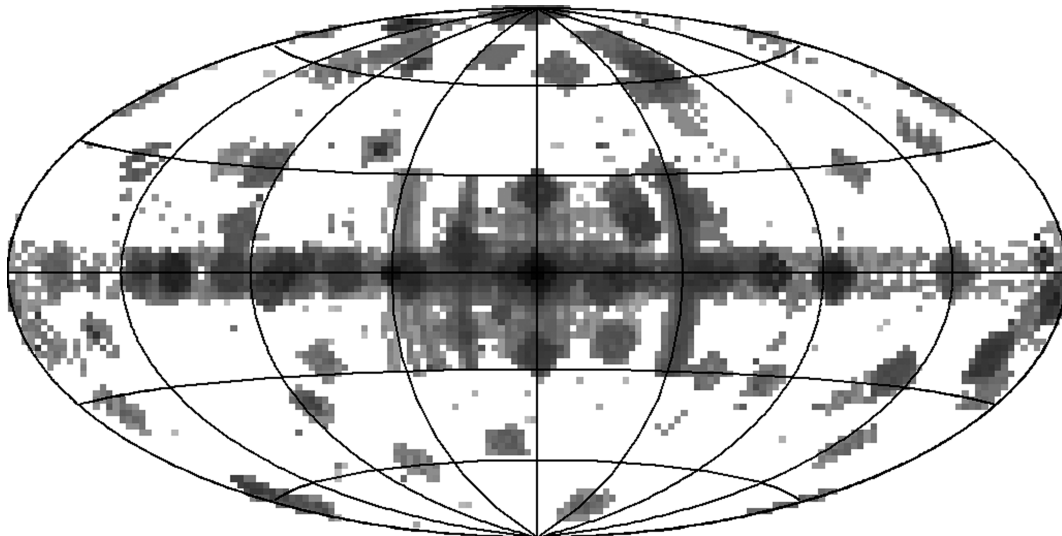


Figure 1. Exposure map (in Galactic coordinates) showing all the observations used in the present analysis. Off-Galactic-plane observations were used for determining the instrument background. For each observation, the effective observing time is added to the pixel in the map containing the pointing direction of the telescope’s axis. The total exposure is about 70 Ms. Pixels are 2° on a side.

the map corresponding to the telescope pointing direction. Similarly, the exposure map is formed by adding the exposure times (see Fig. 1). The ratio of the counts to the exposure map gives the count rate image, which is crudely converted into units of $\text{photon s}^{-1} \text{cm}^2$ using the effective area for an on-axis point source. Such maps will provide a correct point source flux if the telescope is pointed directly towards the source. But given the large size of the SPI FOV ($\sim 30^\circ$ diameter at zero response) and sparse coverage of the sky, ‘light-bucket mapping’ produces rather crude maps, while the procedure itself is very simple and robust. We use light-bucket mapping to get a global surface brightness map or to follow the variations of the surface brightness along and across the Galactic plane with poor angular resolution. Note that in this mode, SPI is used as a collimated instrument and its mask imaging capabilities are not exploited. The net flux (difference between the observed count rate and the predicted background model) crucially depends on the quality of the background model.

3.1.1 Scans along the Galactic plane

In Fig. 2, we show slices of the Galaxy along the Galactic plane in three energy bands. Each slice has a width of 16° perpendicular to the Galactic plane and is centred at $b = 0^\circ$. The step along the Galactic plane is 2° for the two top panels and 4° for the bottom panel.

In the top panel (50–100 keV), three prominent peaks correspond (from left to right) to Cyg X-1, GC and the Crab nebula, respectively. The width of $\sim 30^\circ$ and the complex structure of the peaks near the maximum (clearly visible for Cyg X-1) are due to the presence of the mask and partly due to the intrinsic variability of the sources. The few regions with negative fluxes correspond to observations where the actual background count rate is higher than the model-predicted background described in Section 2.2. Note that the model background was calculated using a set of ‘blank fields’, whose definition is problematic given the large size of the SPI FOV. The sets of blank fields are different in each of the 14 time intervals used in the background modelling (see Section 2.2). For this reason, it is possible that the actual flux from the ‘blank fields’ is higher than that from some patches of the Galactic plane free of strong sources.

The morphology of the slice in the 508–514 keV band,² containing the 511-keV line (Fig. 2, middle panel), is markedly different. With the 2° bins along the Galactic plane, the only prominent feature is the peak at the GC, with the extent along l roughly similar to the extent of the peak near Cyg X-1 at low energies. The peak flux is $\sim 10^{-3} \text{ photon s}^{-1} \text{cm}^2$. As already emphasized, this value is not a precise measure of the true 511-keV flux from the GC region, but it should be accurate to a factor of better than 2 if the source size does not exceed several degrees.

No strong asymmetry of the positive and negative longitude wings of the central peak is apparent in the light-bucket profiles [see, however, Weidenspointner et al. (2008), who report an excess flux for negative longitudes, and Bouchet et al. (2008), who do not find strong evidence for asymmetry]. An excess at negative longitudes $l \sim -25^\circ$ is visible in the light-bucket profile in Teegarden et al. (2005) (their fig. 2). Renormalization of their fluxes to the units used in Fig. 2 suggests an excess at the level of $\sim 1.5 \times 10^{-4} \text{ photon s}^{-1} \text{cm}^2$. In our analysis, the flux at $l \sim -25^\circ$ is essentially consistent with zero. If anything, the profiles shown in Fig. 2 suggest an excess in the 508–514 keV flux at positive longitudes $l \sim 25^\circ$. However, our experiments with ‘alternative’ background models mentioned in Section 2.2 showed that a weak spurious asymmetry (corresponding to a flux excess/deficit of $\sim 10^{-4} \text{ photon s}^{-1} \text{cm}^2$ at $|l| \sim 20^\circ\text{--}25^\circ$) can appear at either negative or positive longitudes. We therefore conclude that, with the present knowledge of the SPI background, light-bucket profiles do not provide compelling evidence for asymmetry in the 508–514 keV flux along the Galactic plane.

Finally in the bottom panel of Fig. 2, the slice of the Galactic plane in the 1804–1813 keV band, containing the 1.8-MeV line of ^{26}Al , is shown. Unlike the 511-keV emission, there is a broad peak (much broader than the SPI response to a point source), centred at the GC. This distribution is qualitatively consistent with the COMPTEL (Plüschke et al. 2001) and earlier *INTEGRAL* results (Wang et al. 2009).

² See Teegarden et al. (2005) for an earlier version of a similar plot.

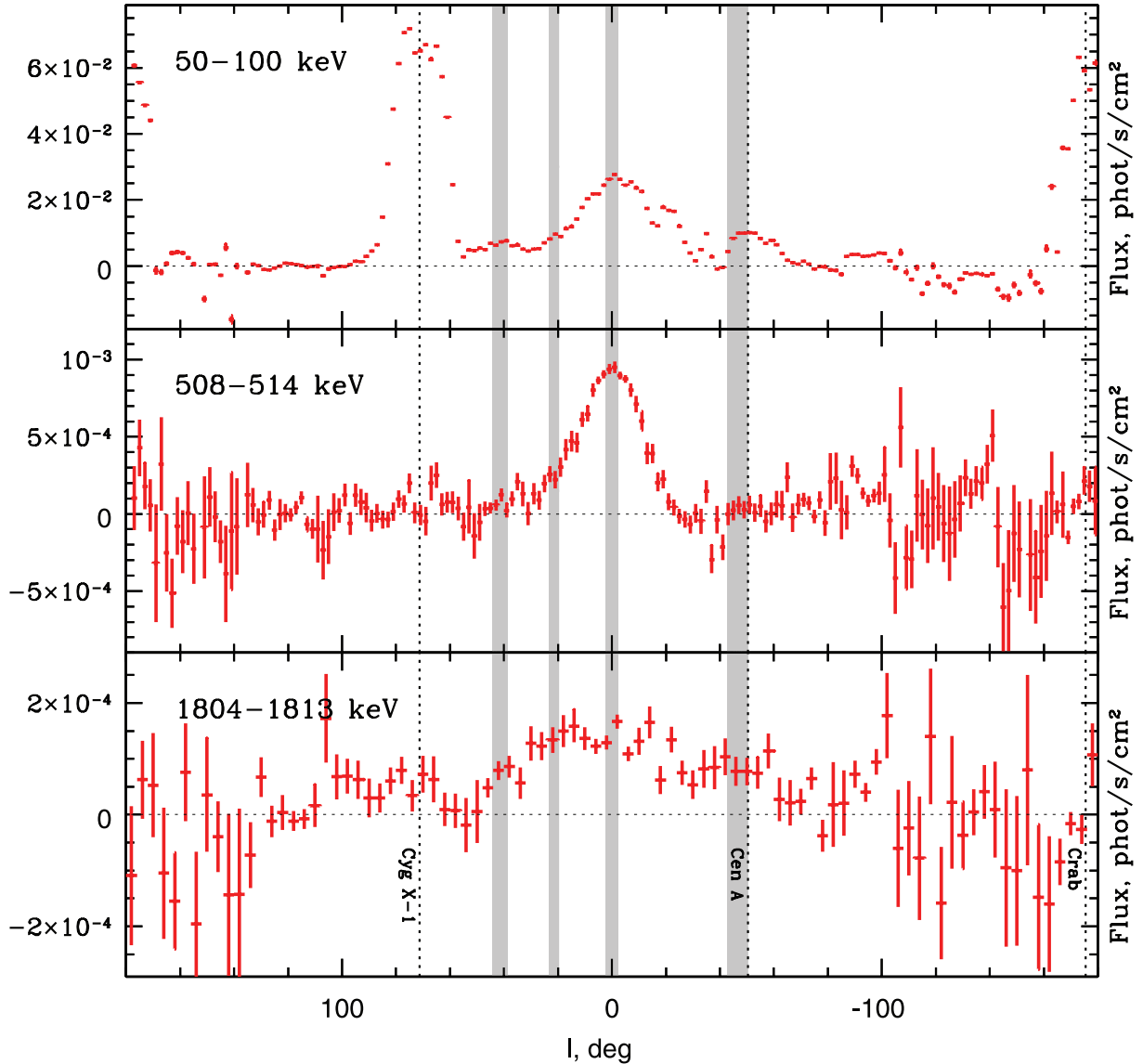


Figure 2. Scans (light-bucket imaging) along the Galactic plane in three energy bands. Fluxes are averaged over 2° bins over l and $\pm 8^\circ$ over b . For the 1804–1813 keV band, the width of the bins along l is 4° . By construction, all points are statistically independent (except through the background subtraction). Vertical grey bars show the positions of the series of scans perpendicular to the Galactic plane discussed in Section 3.1.2. The positions of the Crab nebula, Cyg X-1 and Centaurus A are marked with the vertical dotted lines.

3.1.2 Scans perpendicular to the Galactic plane

A similar approach of light-bucket mapping can be applied to the special scans of the Galactic plane along b performed in 2007–2009. The positions of the scans in l are denoted with the grey vertical lines in Fig. 2. Three out of four scans were made as a sequence of pointings starting and ending $\sim 30^\circ$ away from the plane on either side of it. The pointing direction was changing in $\sim 2^\circ$ steps. The remaining ‘scan’ at $l = 0$ had been done earlier as a set of pointings directly at the plane and $\sim 25^\circ$ above and below the plane. The advantage of making ‘fast’ (taking 10–15 h) scans over a selected region of the sky is that the quality of the background modelling can be verified/improved if typical variations of the detector background occur on longer time-scales.

The scans in the 508–514 keV band in the direction perpendicular to the Galactic plane at $l \sim 0^\circ, 22^\circ, -45^\circ$ are shown in

Fig. 3. The signal is clearly visible at $l \sim 22^\circ$ and is close to zero for $l \sim -45^\circ$. To guide the eye, we have plotted with the black curves the expected light-bucket profiles for the case where the spatial distribution of the flux in the 508–514 keV band follows the ‘bulge’ model described later in Section 3.5. The expected profiles were crudely estimated assuming that the axis of the instrument was moving along b at fixed l , while keeping the position angle fixed. This causes visible asymmetry in the peak of the $l \sim 0^\circ$ profile, reflecting the particular orientation of the SPI coding mask relative to the source. In reality, the observed profiles are combinations of observations with varying position angles and varying l and hence they may differ from the simulated profiles in subtle details. Broadly, the light-bucket imaging shows the overall consistency with a bulge-dominated distribution of the 508–514 keV flux and indicates that the disc emission is weak at $l \sim -45^\circ$.

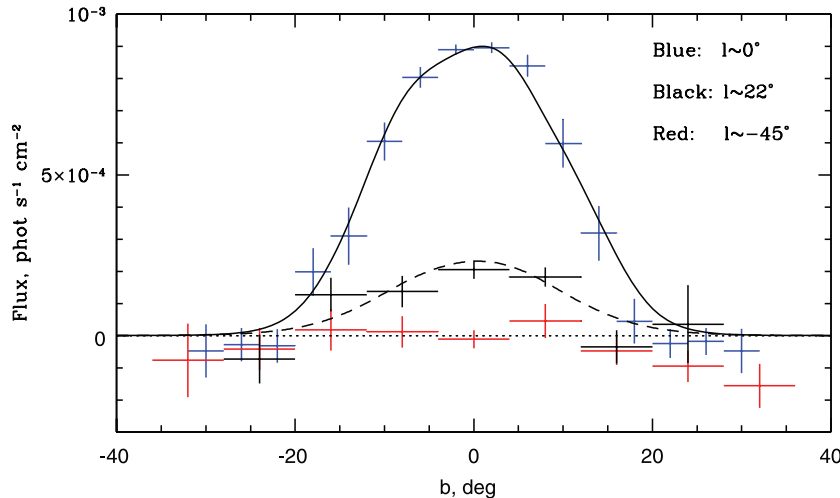


Figure 3. Scans (light-bucket imaging) perpendicular to the Galactic plane at $l \sim 0^\circ, 22^\circ, -45^\circ$ in the 508–514 keV energy band. The solid and dashed curves approximately show the expected profiles at $l \sim 0^\circ$ and 20° if the spatial distribution of the flux in the 508–514 keV band is adequately described by the ‘bulge’ component described in Section 3.5.

3.2 Simple parametric models

We now use a simple function – two-dimensional Gaussian – to model the spatial distribution of the annihilation line emission near the GC. The data collected when the *INTEGRAL* pointing direction was within 30° of the GC were used. Two models were considered:

$$G(l, b) = F_1 \times e^{-\left\{ \frac{l^2 \ln 2}{w_l^2} + \frac{b^2 \ln 2}{w_b^2} \right\}},$$

$$G_D(l, b) = F_1 \times e^{-\left\{ \frac{l^2 \ln 2}{w_l^2} + \frac{b^2 \ln 2}{w_b^2} \right\}} + F_2 \times e^{-\left\{ \frac{b^2 \ln 2}{w_D^2} \right\}}, \quad (2)$$

where $G(l, b)$ is the surface brightness distribution as a function of Galactic longitude and latitude, F is the flux and w_l and w_b are the FWHMs along l and b , respectively. The second model has an additional component that is aimed to account for emission elongated over the Galactic plane. Since only the data within 30° of the GC were used (30° corresponds to the deviation of the SPI axis from the GC), the ‘infinite’ extent of this component over l means that the surface brightness of this component does not decrease much at a distance of $\sim 45^\circ$ from the GC.

To verify the sensitivity of the results to a particular functional form, we also used an exponential law instead of the Gaussian:

$$E(l, b) = F_1 \times e^{-\sqrt{\frac{l^2}{w_l^2} + \frac{b^2}{w_b^2}}},$$

$$E_D(l, b) = F_1 \times e^{-\sqrt{\frac{l^2}{w_l^2} + \frac{b^2}{w_b^2}}} + F_2 \times e^{-\frac{|b|}{w_D}}. \quad (3)$$

For a given pair of w_l and w_b , the model is convolved with the simulated SPI response (Sturmer et al. 2003) and compared with the count rate in the 508–514 keV band in individual detectors during individual observations. The best-fitting value of F_1 for the one-component model or the pair of values F_1 and F_2 for the two-component model is calculated. Here and in all the subsequent analysis, we use simple χ^2 statistics. The problems of using the χ^2 criterion for low photon counting statistics are circumvented following the recipe of Churazov et al. (1996). Namely, the standard deviation associated with the count rate in a given spectral, spatial or time bin is evaluated using the mean count rate averaged over a large number of ‘nearby’ similar bins.

Typical values of χ^2 per degree of freedom for our models are ≈ 1.01 . Given the large number of degrees of freedom ($\sim 250\,000$ = number of detectors times the number of observations) and the

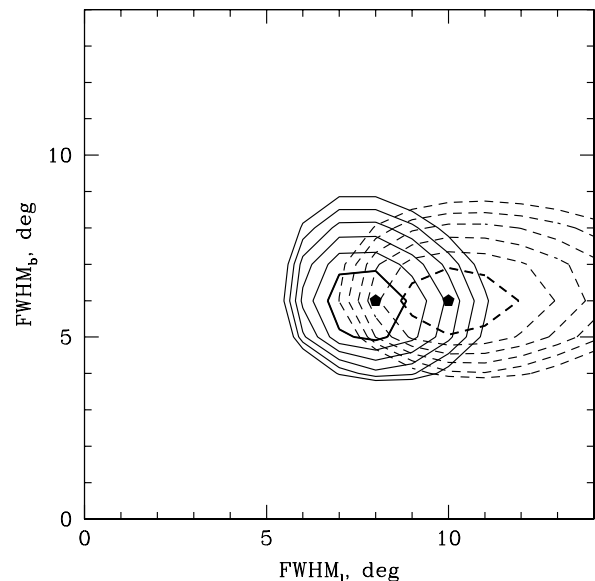


Figure 4. Contours of χ^2 as a function of the FWHM along l and b when the spatial distribution of the 508–514 keV flux is described by a 2D Gaussian. The dashed lines correspond to the pure 2D Gaussian model [$G(l, b)$ in equation 2], while the solid lines correspond to the model $G_D(l, b)$ in equation 2, which includes an additional extended component. Black dots mark the positions of the χ^2 minima. Contours are spaced by $\Delta\chi^2 = 3$. The best-fitting values of the width are $10^\circ \times 6^\circ$ and $7^\circ\text{--}8^\circ \times 6^\circ$ for the first and second models, respectively.

very low signal-to-noise ratio of the annihilation signal in individual observations, this value is not a useful indicator of the ‘absolute’ quality of the model. Instead, the change of χ^2 can be used to compare different models or place constraints on the model parameters.

The resulting contours of χ^2 for both models (as a function of the parameters w_l and w_b) are plotted in Fig. 4. The dashed lines correspond to the one-component model (pure 2D Gaussian), while the solid lines correspond to the two-component model $G_D(l, b)$ (see equation 2). The black dots mark the positions of χ^2 minima. Contours are spaced by $\Delta\chi^2 = 3$. The best-fitting values of the

Table 1. Fitting the 508–514 keV surface brightness with templates and parametric models. Quoted $\Delta\chi^2$ values were calculated relative to the ‘null hypothesis’ of zero flux in the 508–514 keV band over the entire data set. The data within 30° from the GC were used. Quoted fluxes correspond to the integrated model fluxes (with best-fitting normalization) over a $80^\circ \times 80^\circ$ square region around the GC.

Component 1	Spatial template	Component 2	$-\Delta\chi^2$	F_1 (photon $s^{-1} \text{ cm}^{-2}$)	F_2 (photon $s^{-1} \text{ cm}^{-2}$)
Templates described in Section 3.5 with the surface brightness truncated at 10^{-5} of maximum					
Disc	–	–	6837.7	$(2.20 \pm 0.03) \times 10^{-3}$	–
Disc/Hole	–	–	6660.3	$(2.22 \pm 0.03) \times 10^{-3}$	–
Bulge	–	–	8252.4	$(1.12 \pm 0.01) \times 10^{-3}$	–
Bulge	–	Disc	8252.5	$(1.11 \pm 0.03) \times 10^{-3}$	$(2.4 \pm 6.4) \times 10^{-5}$
Bulge	–	Disc/Hole	8252.5	$(1.11 \pm 0.03) \times 10^{-3}$	$(2.0 \pm 6.2) \times 10^{-5}$
Templates with the surface brightness truncated at 10^{-1} of maximum					
Disc	–	–	6964.0	$(1.83 \pm 0.02) \times 10^{-3}$	–
Disc/Hole	–	–	6758.9	$(1.85 \pm 0.02) \times 10^{-3}$	–
Bulge	–	–	8229.1	$(0.97 \pm 0.01) \times 10^{-3}$	–
Bulge ^a	–	Disc	8252.9	$(0.87 \pm 0.02) \times 10^{-3}$	$(2.4 \pm 0.5) \times 10^{-4}$
Bulge	–	Disc/Hole	8253.0	$(0.87 \pm 0.02) \times 10^{-3}$	$(2.3 \pm 0.5) \times 10^{-4}$
<i>G(l, b)</i> and <i>G_D(l, b)</i> models from equations (2) and (3)					
Gaussian $W_l = 10^\circ, W_b = 6^\circ$	–	–	8223.4	$(0.96 \pm 0.01) \times 10^{-3}$	–
Gaussian $W_l = 8^\circ, W_b = 6^\circ$	–	Gaussian, $W_D = 2^\circ$	8260.3	$(0.84 \pm 0.02) \times 10^{-3}$	$(2.9 \pm 0.5) \times 10^{-4}$
Gaussian $W_l = 8^\circ, W_b = 6^\circ$	–	Gaussian, $W_D = 6^\circ$	8262.8	$(0.84 \pm 0.02) \times 10^{-3}$	$(3.1 \pm 0.5) \times 10^{-4}$
Gaussian $W_l = 8^\circ, W_b = 6^\circ$	–	Gaussian, $W_D = 10^\circ$	8263.7	$(0.84 \pm 0.02) \times 10^{-3}$	$(3.3 \pm 0.5) \times 10^{-4}$
Gaussian $W_l = 8^\circ, W_b = 6^\circ$	–	Exponential, $W_D = 2^\circ$	8262.6	$(0.84 \pm 0.02) \times 10^{-3}$	$(3.1 \pm 0.5) \times 10^{-4}$
Gaussian $W_l = 8^\circ, W_b = 6^\circ$	–	Exponential, $W_D = 6^\circ$	8262.6	$(0.84 \pm 0.02) \times 10^{-3}$	$(3.7 \pm 0.6) \times 10^{-4}$
Exponential $W_l = 3^\circ, W_b = 2^\circ$	–	–	8265.4	$(1.01 \pm 0.01) \times 10^{-3}$	–
Exponential $W_l = 3^\circ, W_b = 2^\circ$	–	Gaussian, $W_D = 2^\circ$	8284.1	$(0.93 \pm 0.02) \times 10^{-3}$	$(2.1 \pm 0.5) \times 10^{-4}$

^aThe bulge component of the disc+bulge model is used in the spectral analysis in Section 5.

widths are $10^\circ \times 6^\circ$ (if the one-component model is used) and $\sim 8^\circ \times 6^\circ$ (for the two-component model).³

Clearly, for the pure 2D Gaussian model the data suggest a significant flattening of the distribution towards the plane. If an additional component, extended along the plane, is included (the two-component model in equation 2), then the best-fitting central Gaussian is much more symmetric in l and b . The improvement in χ^2 for the two-component model compared to the one-component model is ~ 40 . The position of the minimum for the two-component model does not depend much on the width of the extended component over b . We tried for the second component $W_D = 2^\circ, 6^\circ$ and 10° as well as an exponential shape $e^{-\frac{|b|}{W_D}}$ instead of the Gaussian, and got essentially the same best-fitting parameters ($8^\circ \times 6^\circ$) for the central Gaussian.

We emphasize here that the presence of the second component does not necessarily imply that the Galactic disc is ‘detected’ but rather that a single symmetric Gaussian/exponential component is not a perfect description of the data.

An exponential shape $e^{-\frac{|l|}{W_l} - \frac{|b|}{W_b}}$ with $W_l \sim 3^\circ$ and $W_b \sim 2^\circ$ can also be used to describe the central component (see Table 1) instead of a Gaussian. In fact, the largest improvement in the χ^2 is achieved when both the central and disc components are described as exponential functions (Table 1). While the difference in the χ^2 between various models (e.g. one-component exponential versus one-component Gaussian) is formally statistically significant, it corresponds to less than a 1 per cent change in the $\Delta\chi^2$ value relative to the ‘null hypothesis’ of a zero flux in the 508–

514 keV band over the entire data set. At this level, a particular value of $\Delta\chi^2$ for a given model might be sensitive to the subtle features of the data set. Our experiments with different background models have indeed shown that the ranking of models in terms of χ^2 can slightly vary. For example, the ranking of the Gaussian + Gaussian and Gaussian + exponential models in Table 1 can change depending on the particular background model.

Despite the difference in the functional forms, the flux in the central component does not depend strongly on the model used; it varies between 8.4×10^{-4} and 9.3×10^{-4} photon $s^{-1} \text{ cm}^{-2}$ for all two-component models.

3.3 Position of the centroid

Using the one-component exponential model (the first model in equation 3) with $W_l = 3^\circ$ and $W_b = 2^\circ$, we tried to vary the centroid of the distribution over a few degrees around the GC and calculated the changes in the χ^2 . The best-fitting position is at $(l, b) = (-0.1, -0.2)$ and the minimal χ^2 differs from the value at $(l, b) = (0, 0)$ by 2.3. While this means that formally the statistics of accumulated data is already sufficient to measure sub-degree shifts of the centroid, we believe that systematic uncertainties and the obvious crudeness of the spatial model preclude any firm conclusion. We can conservatively conclude from this exercise that the position of the centroid is consistent within ~ 0.2 with the position of the dynamic centre of the Milky Way.

3.4 Tilted Gaussian

Higdon et al. (2009) have suggested that a significant fraction of positrons are annihilating in a ‘tilted disc’ of neutral gas inside the

³ Note that we used a grid over FWHM values with a 1° step, and a $7^\circ \times 6^\circ$ Gaussian gives almost the same χ^2 as the best-fitting $8^\circ \times 6^\circ$ Gaussian.

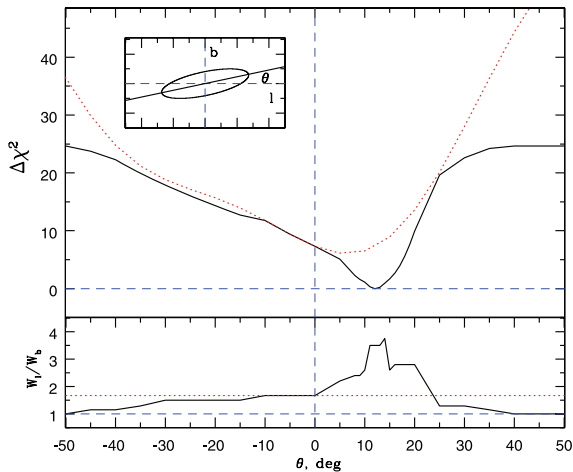


Figure 5. χ^2 as function of the tilt θ of a two-dimensional Gaussian (solid black line). The tilt is measured relative to the Galactic plane. Positive values of the tilt correspond to the major axis pointing towards positive b at negative l . For each value of the tilt, the best-fitting values of the FWHM in two dimensions were identified on a crude FWHM grid with steps of $\sim 1^\circ$. The ratio of the FWHMs (W_l/W_b) is shown in the bottom panel. The minimum of the χ^2 is achieved at $\theta = 12^\circ$ and $W_l = 14^\circ$, $W_b = 4^\circ$. The large variations of the W_l/W_b ratio are owing to the crudeness of the grid and a very shallow minimum in the function $\chi^2(W_l/W_b)$ for a given θ . As $|\theta|$ increases, the Gaussian converges to a symmetric structure ($W_l/W_b \approx 1$). For comparison, the red dotted line shows the χ^2 as a function of the tilt if W_l and W_b are fixed at their best-fitting values of 10° and 6° , respectively, for $\theta = 0$.

central 3-kpc region of the Galaxy. This ‘tilted disc’ is one of the components of the Ferrière et al. (2007) model of the interstellar gas distribution in the innermost part of the Milky Way, based on earlier results of Liszt & Burton (1980) (see also Liszt & Burton 1996). The tilted disc (see fig. 4 in Ferrière et al. 2007) in projection to the sky plane has an apparent size of $\sim 18^\circ \times \sim 5^\circ$ and is tilted by $\sim 30^\circ$ with respect to the Galactic plane. Since the extent of the disc in l and b resembles the dimensions of the 511-keV source, Higdon et al. (2009) suggest that the positrons reach the disc and annihilate there.

To test further the tilted disc model, we fit the data with a two-dimensional Gaussian allowing for rotation of the major axis. The results are shown in Fig. 5. The best-fitting rotation angle and the widths of the Gaussian in two directions are $\theta \sim 12^\circ$ and $W_l = 14^\circ$, $W_b = 4^\circ$, respectively. The improvement in χ^2 compared to $\theta = 0^\circ$ (and $W_l = 10^\circ$, $W_b = 6^\circ$) is $\Delta\chi^2 \approx 7$. As discussed already, the values of $\Delta\chi^2$ of the order of a few are formally statistically significant if the errors are due to counting Poisson noise only. The total change of the χ^2 when a two-dimensional Gaussian is added to the model is ~ 8000 . Comparing these numbers, it is clear that even modest systematics in the data could affect precise derivation of the source spatial characteristics. Taking the results shown in Fig. 5 at face value, a marginally significant improvement in the fit is possible if the annihilation region is tilted by $\sim 12^\circ$ with respect to the Galactic plane.

As $|\theta|$ increases beyond 25° , the Gaussian converges to an almost symmetric structure. The tilt of $\theta \sim 30^\circ$ corresponds to $\Delta\chi^2 \approx 23$ for an almost symmetric Gaussian with $W_l = 9^\circ$ and $W_b = 7^\circ$. We therefore conclude that a version of the tilted disc of Ferrière et al. (2007) is not particularly favoured by SPI data compared to a structure with zero tilt. However, moderate values of $\lesssim 20^\circ$ of the tilt are allowed by the SPI data.

3.5 Decomposition using plausible templates

The simple light-bucket imaging and parametric fitting of the 508–514 keV flux done in Sections 3.1 and 3.2 suggest that a reasonable description of the data in the central radian could be achieved with an almost symmetric Gaussian at the centre and a more extended component along the plane. The stellar bulge and stellar disc are the most obvious structural components of the Galaxy that qualitatively fit this description. In fact, there are plenty of disc-like structures (cold gas, massive stars, cosmic ray-induced gamma-ray flux, etc.) and very few components that show a prominent peak at the GC. One of the known centrally peaked distributions is that of the NIR light, which is a tracer of the old stellar population of the Galaxy. For this reason, we decided to restrict our analysis to three simple templates, corresponding to stellar components of the Milky Way, adopted from López-Corredoira, Cabrera-Lavers & Gerhard (2005) and shown in Fig. 6:

- (i) disc (equations 2–5 in López-Corredoira et al.);
- (ii) disc with a hole (equations 6–7 in López-Corredoira et al.);
- (iii) bulge (see section 3 in López-Corredoira et al.).

This is by no means a comprehensive list of possible templates [see e.g. Knödseder et al. (2005) for a systematic analysis of various templates]. However, the hope is that these spatial templates will capture the most basic properties of the 508–514 keV flux distribution, even if the physical motivation is questionable or the details of shape are not correct.

We also used slightly modified (truncated) versions of these templates: for each template we set to zero the surface brightness in all regions where it is smaller than 10 per cent of the peak value. The motivation behind this modification is an attempt to have a template that has a bulge or disc-type morphology at high surface brightness but lacks the extended low surface brightness regions, which might make a significant contribution to the total flux.

For a given set of templates, the surface brightness for each template is convolved with the simulated SPI response (Sturmer et al. 2003) yielding an expected count rate in the 508–514 keV band in individual detectors during individual observations. The best-fitting normalizations of the templates are then calculated in

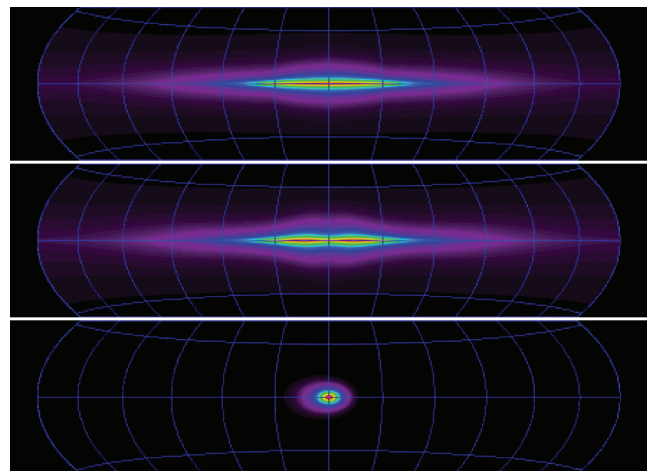


Figure 6. The model templates used for fitting the data in the 508–514 keV band (from top to bottom): disc, disc with a hole and bulge. The projected surface brightness distributions shown are based on the three-dimensional models of stellar density distribution adopted from López-Corredoira et al. (2005).

order to minimize the χ^2 deviation between the raw data and the model.

The χ^2 values for the various spatial models are given in Table 1. The fluxes quoted in Table 1 are the integrated model fluxes (with best-fitting normalization) over an $80^\circ \times 80^\circ$ square region around the GC. The choice of the region for the calculation of the integrated model flux is rather arbitrary. The $80^\circ \times 80^\circ$ region is not uniformly covered by observations, and areas with the smallest errors (largest exposures) dominate in the determination of the best-fitting normalization. On the other hand, underexposed (or even not observed at all) areas can still provide a significant contribution to the total integrated flux. An example of a clear overestimation of the flux due to this effect is seen for the pure ‘disc’ models in Table 1. These models have poor χ^2 , but predict a large integrated flux, since their normalization is largely set by the innermost bright region of the Galaxy. This becomes an especially severe problem when dealing with fluxes integrated over very large areas (e.g. the flux from the entire Galactic disc). For this reason, we quote fluxes integrated over the $80^\circ \times 80^\circ$ region rather than from the whole Milky Way.

Table 1 strongly suggests that the spatial distribution of the 508–514 keV flux in the inner region of the Galaxy is more extended along the Galactic plane than perpendicular to it. This is clear from the parameters of the single-component parametric models (see also Fig. 4) and from the comparison of the χ^2 values for the one-component and two-component (e.g. two Gaussians) models.

Among the one-component models, the exponential model has a slightly better χ^2 than the Gaussian model or the bulge model. For the two-component models, the exponential bulge + Gaussian disc has the smallest χ^2 among the set of models considered here. It is clear that (i) the true distribution of the 508–514 keV flux is likely more complicated than any of the models used and (ii) the relatively modest (although statistically significant) changes in the χ^2 among different models (containing the bulge component) suggest that the basic properties of the distribution are captured by our models.

The uncertainty in the choice of the spatial model directly translates into the uncertainty of the 508–514 keV flux. In particular, the total flux of the bulge component varies among all two-component models (both parametric and based on templates) from 0.84×10^{-3} to 1.11×10^{-3} photon $s^{-1} \text{ cm}^{-2}$. At the same time, the total bulge + disc flux (integrated over the $80^\circ \times 80^\circ$ region) varies from 1.10×10^{-3} to 1.14×10^{-3} photon $s^{-1} \text{ cm}^{-2}$.

Since some of the spatial templates used in Table 1 are projections of the three-dimensional models (based on stellar distribution), it is easy to recalculate the observed flux F into the total luminosity L of the corresponding component as $L = 4\pi D^2 \times F$. Here D depends on the three-dimensional distribution of the volume emissivity and on the region used to calculate the flux F . The values of D are given in Table 2. Using the effective distances from Table 2 for the templates truncated at 10 per cent of the maximal surface brightness, the

Table 2. Effective distance D needed to recalculate the observed flux from the $80^\circ \times 80^\circ$ region around the GC into the luminosity for different spatial components. Two columns correspond to different cut-offs in the surface brightness distribution of each component (relative to the maximal surface brightness of this component).

Spatial template	Effective distance (kpc)	
	Cut-off = 10^{-5}	Cut-off = 0.1
Disc	7.74	8.98
Disc/Hole	7.79	8.99
Bulge	5.89	6.93

total luminosity of the bulge component is $\sim 5.0 \times 10^{42}$ photon s^{-1} , while the total disc luminosity is $\sim 2.3 \times 10^{42}$ photon s^{-1} . As noted above, the resulting luminosities rely on the model 3D distribution and for this reason they are model dependent.

4 ^{26}Al DECAY

^{26}Al is one of the obvious and accountable sources of the positrons in the Galaxy (see e.g. Diehl et al. 2008). This radioactive isotope with the half-life time of 7.17×10^5 yr is produced by massive stars, which primarily occupy the disc of the Galaxy. The positrons are produced in 81.7 per cent of decays, with the mean energy of 543 keV; in 99.8 per cent, a 1.809-MeV photon is emitted.⁴ Assuming that the fraction of positrons forming positronium is f_{ps} (see Section 5), the fluxes in the 511-keV and 1.8-MeV lines per one positron produced via ^{26}Al decay are

$$\begin{aligned} F_{511} &= 0.817 \left[(1 - f_{\text{ps}}) + \frac{1}{4} f_{\text{ps}} \right] \times 2 = 1.63 \left[1 - \frac{3}{4} f_{\text{ps}} \right], \\ F_{1.8} &= 0.998. \end{aligned} \quad (4)$$

Here we assume that (i) the fraction of para-positronium is 1/4 and (ii) all positrons annihilating without formation of positronium (fraction $1 - f_{\text{ps}}$) produce a narrow 511-keV line. The factor 2 in the above expression accounts for the two photons produced in two-photon annihilation. Therefore, $F_{511} = 0.409, 0.471$ and $1.637 \times F_{1.8}$, for $f_{\text{ps}} = 1, 0.95$ and 0, respectively (see Section 5 for details).

It is interesting to compare this relation with the fluxes obtained from the light-bucket images in the 508–514 and 1804–1813 keV energy bands, which should contain most of the 511- and 1809-keV line fluxes, unless the lines are strongly broadened. Shown in Fig. 7 is a light-bucket longitude scan of the Galactic plane over the region $l = \pm 60^\circ$. The blue thick crosses show the flux in the 508–514 keV band, while the thin red crosses show the observed flux in the 1804–1813 keV band scaled by a factor of 0.409. These red crosses correspond to the expected 511-keV line flux arising from ^{26}Al decay under the assumption that 100 per cent of positrons annihilate through the formation of positronium. It will be observed later in Section 5 that this assumption is supported by spectral data. Clearly, the high 511-keV line flux from the GC region cannot be explained by ^{26}Al decay (unless the positrons produced in the disc are somehow transported to the central region; see e.g. Prantzos 2006).

One can use the same set of templates as in Section 3.5 and repeat the analysis for a set of energies to obtain the spectrum associated with each spatial component. We did this using the disc+bulge model, which was applied to all observations with the *INTEGRAL* pointing direction within 30° from the GC. Since we do not explicitly account for compact sources in this procedure, the low energy parts of the spectra obtained may not be reliable. However, near the 511-keV and 1.8-MeV lines the contribution of individual sources should not be crucial. Nevertheless, this simplifying assumption should be kept in mind when interpreting the resulting spectra, shown in Fig. 8.

The top row in Fig. 8 shows the spectrum of the bulge component in the vicinity of the 511-keV and 1.8-MeV lines. The red line in the top-left panel shows the best-fitting model (Gaussian at 511 keV and ortho-positronium continuum; see Section 5 for details). The flux in the 511-keV line in this model is $F_{511} = (0.84 \pm 0.03) \times 10^{-3}$ photon $s^{-1} \text{ cm}^{-2}$. Note that this flux was obtained

⁴ <http://www.nndc.bnl.gov/mird/>

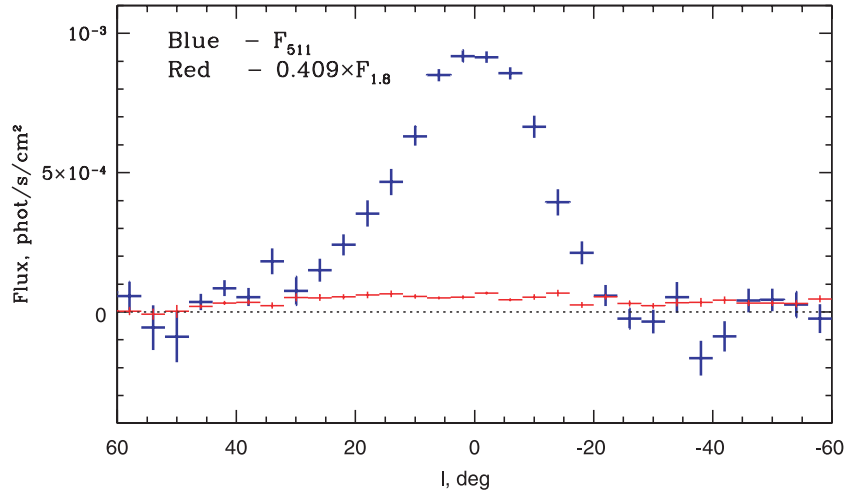


Figure 7. Expected contribution of positrons produced by ^{26}Al decay to the annihilation line flux in the vicinity of the GC. The light-bucket technique was used (see Section 3.1). The slice has a width of 16° perpendicular to the Galactic plane and is centred at $b = 0^\circ$. The step along the Galactic plane is 4° . The measured flux in the 508–514 keV band is shown with blue crosses; the red crosses show the flux in the 1804–1813 keV band scaled by a factor of 0.409, which is the expected 511-keV line flux arising from ^{26}Al decay under the assumption that 100 per cent of positrons annihilate through the formation of positronium. It will be observed in Section 5 that this assumption is supported by spectral data. Clearly, the 1804–1813 keV flux arising from the GC region is far too low to explain the observed 511-keV line by the local ^{26}Al decay.

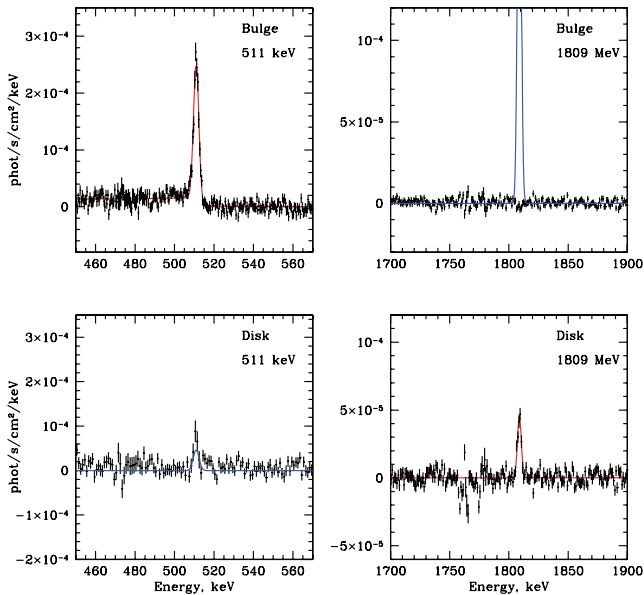


Figure 8. Spectra of the bulge (top row) and disc (bottom row) near 511 and 1809 keV, obtained using the decomposition of the data with the two-component disc + bulge model. The red line in the top-left panel shows the best-fitting model (Gaussian at 511 keV and ortho-positronium continuum; see Section 5 for details). The flux in the 511-keV line in this model is $F_{511} = 0.84 \times 10^{-3} \text{ photon s}^{-1} \text{ cm}^{-2}$. The blue curve in the top-right panel shows a Gaussian line at 1.809 MeV. The flux in the Gaussian was calculated as $F_{1.8} = F_{511}/0.409$, corresponding to the assumption that all positrons are produced by ^{26}Al decay and the fraction of annihilations via positronium is $f_{\text{ps}} = 1.0$ (see equation 4 and Section 5). The bottom row shows the spectrum of the disc component. In contrast to the bulge spectrum, the 1.8-MeV line is very prominent in the spectrum (bottom-right panel). The red line shows the best-fitting Gaussian at 1.809 MeV, with flux $F_{1.8} = 4.1 \times 10^{-4} \text{ photon s}^{-1} \text{ cm}^{-2}$. The blue line in the bottom-left panel now shows a 511-keV line with flux $F_{511} = 0.409 \times F_{1.8}$.

from the spectral analysis and it differs slightly from the ‘bulge’ flux obtained from the analysis of the count rate in the 508–514 keV band, quoted in Table 1. The value F_{511} was then recalculated into the expected flux in the 1.8-MeV line using the relation $F_{1.8} = F_{511}/0.409$, corresponding to the assumption that all positrons are produced by ^{26}Al decay and the fraction of annihilations via positronium is 100 per cent (see equation 4 and Section 5). A line with the resulting flux $F_{1.8}$ is plotted in the top-right panel as a Gaussian line centred at 1.809 MeV. Clearly, such a strong line at 1.8 MeV is in stark contrast to the data, which show no evidence for 1.8-MeV emission in the bulge spectrum.

The bottom row in Fig. 8 shows the disc component spectrum in the vicinity of the 511-keV and 1.8-MeV lines. In contrast to the bulge spectrum, the 1.8-MeV line is now very prominent in the data (bottom-right panel). The red line shows the best-fitting Gaussian at 1.809 MeV with flux $F_{1.8} = (4.1 \pm 0.5) \times 10^{-4} \text{ photon s}^{-1} \text{ cm}^{-2}$. The blue line in the bottom-left panel now shows a 511-keV line with flux $F_{511} = 0.409 \times F_{1.8}$. The data do show the presence of a 511-keV line in the disc component, although our experiments with the alternative background models and various spatial patterns demonstrate that the parameters of the line near 511 keV are not determined reliably.

Thus, Fig. 8 suggests that with the two-component spatial bulge+disc model, we reach the following conclusions.

(i) The strong 511-keV line is confined to the bulge component, with a flux of $0.84\text{--}0.93 \times 10^{-3} \text{ photon s}^{-1} \text{ cm}^{-2}$ and the corresponding 511-keV line production rate of $\sim 0.5 \times 10^{43} \text{ photon s}^{-1}$ (equivalent to an annihilation rate of $\sim 10^{43}$ positrons per second if the positronium fraction is 100 per cent).

(ii) The 1.8-MeV line is on the contrary confined to the disc component. The flux (model flux integrated over an $80^\circ \times 80^\circ$ square region around the GC) is $4.1 \times 10^{-4} \text{ photon s}^{-1} \text{ cm}^{-2}$, corresponding to an ^{26}Al mass of $\sim 2.8 M_\odot$ within the same region (see also Wang et al. 2009).

(iii) An upper limit on the ratio of the 1.8-MeV and 511-keV line fluxes in the bulge component is $F_{1.8}/F_{511} < 0.027$ (2σ), which is two orders of magnitude lower than the expectation for the positrons

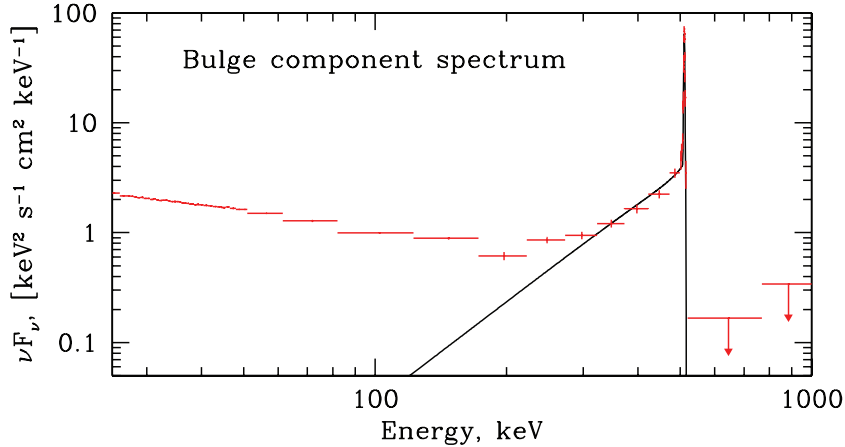


Figure 9. Broad 30–1000 keV spectrum of the bulge component of the two-component spatial model described in Section 3.5. The black line shows the spectral model consisting of a Gaussian line at 511 keV and the associated ortho-positronium continuum, with the parameters given in Table 3.

being produced by ^{26}Al decay and $f_{\text{ps}} \sim 1$ (even if $f_{\text{ps}} = 0$, the ratio is still ~ 20 times lower than the expectation).

(iv) The ratio of the 1.8-MeV to 511-keV line fluxes in the disc component $F_{511}/F_{1.8} = 0.56 \pm 0.2$ is consistent with ^{26}Al decay producing the positrons, although the large uncertainty in the 511-keV flux in the disc component precludes a firmer conclusion.

5 SPECTRA

The emission seen by SPI from the central radian of the Galaxy contains contributions of many spatially and physically different components, e.g. bright compact sources, unresolved weak sources, emission coming from the disc, etc. The clean ‘decoupling’ of 511-keV and 1.8-MeV emission into the bulge and disc components made in Section 4 strongly suggests that analysing the spectrum associated with the bulge component is advantageous for understanding the nature of 511-keV emission. Indeed, the disc component might absorb some physically unrelated emission (like the 1.8-MeV line or the continuum at hundreds of keV, which may be attributed to the interaction of cosmic rays with the ISM), and the remaining bulge component spectrum should be ‘cleaner’. The main disadvantage of this approach is that the significance of all features goes down once two spatial components with free normalizations are allowed (see e.g. Table 1 – the error on the 508–514 keV flux from the bulge is twice as large in the bulge + disc model as in the pure bulge model). In spite of the increased uncertainties, we choose to apply the subsequent spectral analysis to the bulge component of the bulge + disc model. The broad-band spectrum of this component is shown in Fig. 9. In the bulge component spectrum, the flux at energies above 511 keV is consistent with zero, suggesting that a broad-band continuum does not contribute much around 500 keV. At energies lower than ~ 300 keV, a broad-band continuum is clearly visible. We know many compact sources that contribute to this continuum, for example 1E 1740.7–2942 or GRS 1758–258. They have hard spectra around 100 keV, but decline strongly at higher energies, making a small contribution at ~ 500 keV.

5.1 In-flight annihilation

As a rule, the positrons produced by any plausible physical process are born ‘hot’, i.e. with kinetic energy of the order of or higher than the rest energy. For positrons with energy $E_{\text{kin}} \leq m_e c^2$, the

rate of Coulomb and ionization energy losses dominates over the annihilation rate and the positrons first slow down before they have a chance to annihilate.

In some scenarios (e.g. dark matter annihilation or production of positrons in the vicinity of relativistic compact objects), the initial energy of the positrons can be much higher than $m_e c^2$. As discussed by Aharonian & Atoyan (1981a,b), Beacom & Yüksel (2006) and Sizun, Cassé & Schanne (2006), if $E_{\text{kin}} \gg m_e c^2$, the energy losses and annihilation rates differ by only a factor of ~ 10 and a substantial fraction of high energy positrons annihilate during the slow-down process. These high energy positrons will form a broad feature at a mean energy of $\sim m_e c^2 + E_{\text{kin}}/2$, while the slowed-down positrons will annihilate at much lower energies and will power a narrow 511-keV line. Thus, a high energy (above 511-keV) component is expected to be present in the spectrum, with the relative intensity with respect to the narrow 511-keV line depending on the initial positron energy E_{kin} and the ionization state of the ISM. The latter controls the contribution of the ionization and Coulomb losses to the total energy loss rate.

Shown in Fig. 10 are the observed spectrum of the bulge component and the expected in-flight annihilation spectrum⁵ for a neutral (solid) and ionized (dashed) medium. The difference in normalization is due to the larger energy losses in the ionized medium, which increases the fraction of the slowed-down positrons at the expense of in-flight annihilation. The fraction of slowed-down positrons annihilating via positronium formation was set to $f_{\text{ps}} = 0.97$. The spectra shown correspond to initial positron energies of 1, 3, 5, 10, 50 and 100 MeV. No significant flux above 511 keV is observed by SPI in the bulge component (for the two-component model described in Section 3.5), and in Fig. 10 we show the corresponding 2σ upper limits. Evidently, the SPI data above 511 keV do not place tight constraints on the initial energy of positrons. As discussed by Beacom & Yüksel (2006) and Sizun et al. (2006), tighter constraints come from COMPTEL data combined with the SPI measurements of the 511-keV line flux and f_{ps} , restricting E_{kin} to less than 3–7.5 MeV, depending on the ionization state of the medium [see also Aharonian & Atoyan (1981a) for similar calculations based on earlier measurements of the gamma-ray flux from the GC region].

⁵ The expected spectrum in addition to the in-flight annihilation includes the internal bremsstrahlung component (Beacom, Bell & Bertone 2005; Beacom & Yüksel 2006).

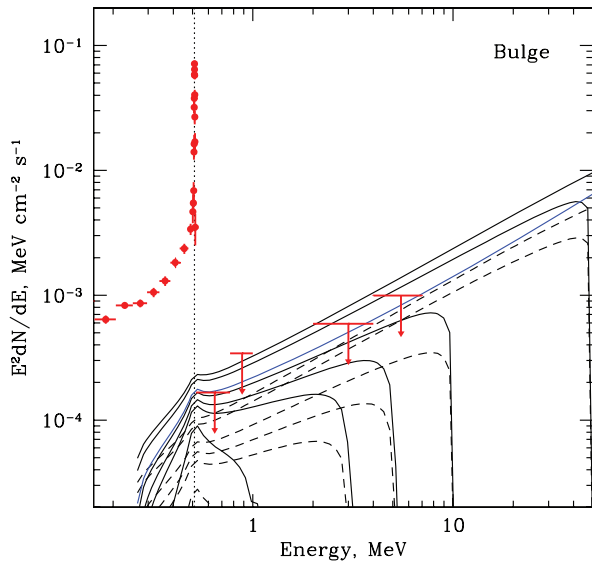


Figure 10. Expected in-flight annihilation spectrum for a neutral (solid) and ionized (dashed) medium, normalized to the 511-keV line flux observed in the bulge component of the bulge+disc model. The initial energy of positrons is 1, 3, 5, 10, 50 and 100 MeV. The upper limits are 1σ values. Both the in-flight annihilation and internal bremsstrahlung components are included in the shown spectra, calculated following Aharonian & Atoyan (1981b) and Beacom & Yüksel (2006). The blue solid line shows the pure in-flight annihilation spectrum (without internal bremsstrahlung) for 100-MeV positrons in a neutral ISM.

The limits on the bulge flux above 511 keV do not strongly constrain the amount of cosmic rays in the bulge, which may produce positrons via π^+ production. Indeed, the same cosmic rays would also produce a comparable amount of π^0 , which would be visible as gamma-ray emission with a peak around 100 MeV. As discussed by e.g. Aharonian & Atoyan (2000), the total gamma-ray flux from the inner Galaxy associated with π^0 decay does not exceed $\sim 10^{-4}$ photon $\text{cm}^{-2} \text{s}^{-1} \text{sr}^{-1}$, corresponding to a flux of $\lesssim 10^{-5}$ photon $\text{cm}^{-2} \text{s}^{-1}$ within the bulge area (assuming a solid angle of the bulge of $\sim 0.1 \text{sr}$). This is about two orders of magnitude smaller than the observed bulge flux of 10^{-3} photon s^{-1} in the annihilation line. The curves shown in Fig. 10 are scaled by the observed rate of positron production, and they approximately match the SPI upper limits (for the initial energy of positrons of ~ 100 MeV). Therefore, the SPI upper limits on the in-flight annihilation of positrons constrain the π^+ production rate to be less than $\sim 10^{-3} \text{s}^{-1}$. Since the π^+ and π^0 production rates by the same cosmic rays are comparable, it is obvious that observations of ~ 100 -MeV gamma rays provide much tighter constraints on the amount of cosmic rays in the bulge.

5.2 Annihilation in a static ISM

We now proceed with spectral fitting of the 511-keV line and ortho-positronium continuum below 511 keV. The simplest possible model is a combination of a Gaussian at 511 keV to describe two-photon annihilation and the three-photon spectrum of Ore & Powell (1949). The line normalization, energy and width and the normalization of the ortho-positronium continuum are free parameters of the model. The best-fitting values of these parameters are given in Table 3. The values agree well with the previously reported SPI results (e.g. Churazov et al. 2005; Jean et al. 2006). Minor variations of the parameters among different publications can be

Table 3. Best-fitting parameters of the bulge component spectrum (for the bulge + disc model) in the 400–600 keV band. The quoted errors are 1σ errors for a single parameter of interest. For the best-fitting model, $\chi^2 = 401.8$ for 395 degrees of freedom.

Parameter	Value
Energy (keV)	510.985 ± 0.049
Width (FWHM) (keV)	2.40 ± 0.16
Flux in 511-keV line	$(0.84 \pm 0.03) \times 10^{-3}$
Positronium fraction, f_{ps}	1.00 ± 0.02

attributed to the different background models and differences in the spectra extraction procedures.

Adding a power-law component does not improve the χ^2 or affect the parameters of the model when the data in the 400–600 keV band are considered. As mentioned at the beginning of Section 5, this is true when the bulge component of the bulge + disc model is considered. It seems that the contribution of known compact sources is relatively small around 500 keV, while the hard continuum associated with the interactions of cosmic rays with the gas largely goes into the disc component.

As discussed by Bussard, Ramaty & Drachman (1979) (see also Guessoum, Ramaty & Lingenfelter 1991; Guessoum, Jean & Gillard 2005), the effective linewidth and the positronium fraction principally depend on the temperature and the ionization state of the medium. This dependence is shown in the left-hand panel in Fig. 11 (adopted from Churazov et al. 2005), where the relation between the effective width of the line and the fraction of positrons annihilating via positronium formation is shown together with the observed parameters taken from Table 3. Compared to the previously reported version of the same plot (Churazov et al. 2005), the uncertainties on the positronium fraction have decreased substantially, but the principal result remains the same: in terms of a single-phase ISM model, a combination of the effective width⁶ of the line of ~ 2.4 keV and the positronium fraction $f_{\text{ps}} \sim 1$ can be explained either with a gas of temperature in the range from 7500 to 4×10^4 K or with a much cooler gas at ~ 100 K. In both cases, the ionization degree should be at the level of a few per cent. While formally the higher temperature solution seems to be preferable because of the large positronium fraction, our experiments with background (and spatial) models have shown that we can drive the positronium fraction down to 96–97 per cent, making the low-temperature solution more consistent with the data.

Of course, the shape of the annihilation spectrum in an ISM of a given temperature and ionization state cannot be fully described by a combination of a Gaussian and the ortho-positronium continuum. Indeed, in-flight annihilation typically contributes a broader component to the 511-keV line than the two-photon annihilation of thermalized positrons. We therefore ran a grid of models for a set of ISM temperatures and ionization states, calculated the expected annihilation spectra using the same procedure as in Churazov et al. (2005) and compared them with the observed bulge spectrum. The initial energy of positrons was set to $E_{\text{kin}} = 500$ keV.

The results are insensitive to the particular value of initial energy unless $E_{\text{kin}} \gg m_e c^2$ or instead E_{kin} is much lower than a fraction of keV. Contours of χ^2 values with an increment $\Delta\chi^2 = 3$ are shown in the right-hand panel of Fig. 11. The minimum of χ^2 achieved at

⁶ The effective width eFWHM (Guessoum et al. 1991) of the line is defined as an energy interval containing 76 per cent of the line photons.

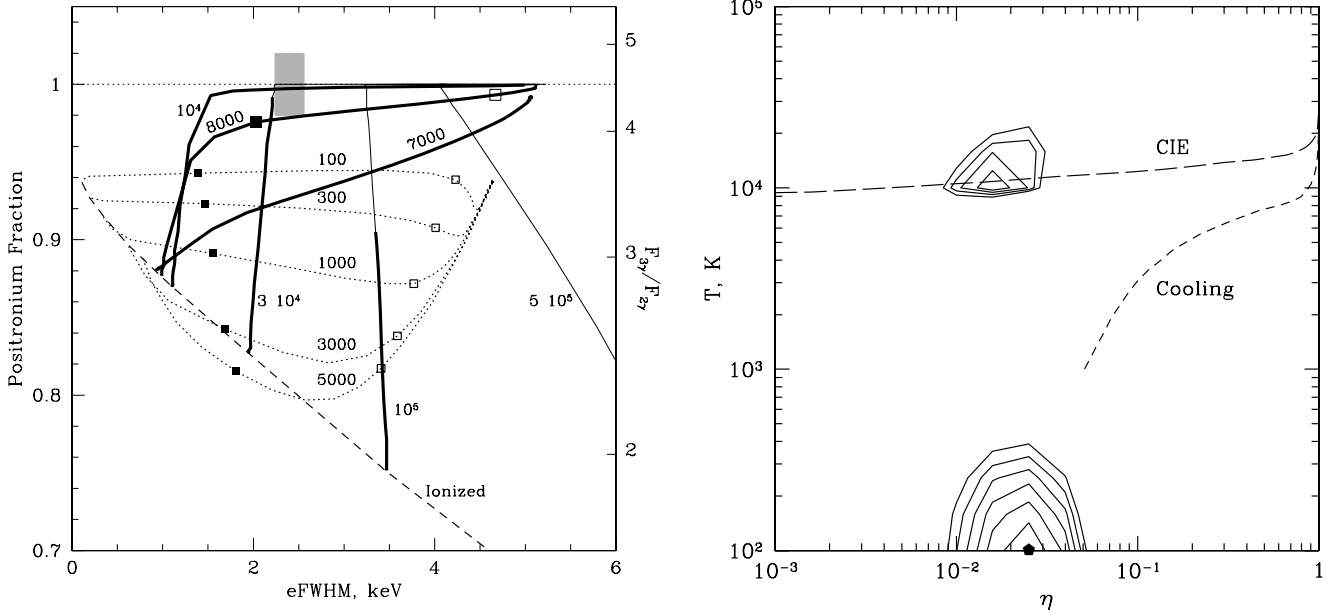


Figure 11. Left: the effective FWHM of the 511-keV line versus the fraction of annihilations through positronium formation (the curves are adopted from Churazov et al. 2005). The grey area is the width and the positronium fraction measured by SPI. There are two groups of theoretical curves: cold – $T \leq 5000$ K (dotted lines) and warm/hot – $T \geq 7000$ K (solid lines). The temperature is fixed for each curve (the labels next to the curves), but the ionization fraction varies so that plasma changes from neutral to completely ionized along the curve. For cool temperature curves and for the 8000-K curve, the points corresponding to the ionization degree of 0.01 and 0.1 are marked with the open and solid squares, respectively. Each high temperature curve has two regimes, shown by thin and thick solid lines, respectively. Thin (thick) lines correspond to ionization fractions smaller (larger) than expected for collision-dominated plasma at this temperature. The over-ionized state (the regime shown by thick lines) is more natural for the ISM than the under-ionized one (thin lines). Finally, the dashed line shows the relation between the linewidth and positronium fraction for a completely ionized plasma as a function of temperature. Right: contours of χ^2 for a grid of models over the static ISM temperature T and ionization degree $\eta \equiv n_e/(n_e + n_H)$. The initial energy of positrons is set to 500 keV. The χ^2 is calculated for the 400–600 keV range for the spectrum of the bulge component in the bulge + disc model. The minimum of $\chi^2 = 402.4$ achieved at $T = 10^2$ K and $\eta = 0.025$ is marked with a black dot. Contours are plotted with an increment $\Delta\chi^2 = 3$. There are two pronounced minima: at $T \sim 100$ and $\sim 10^4$ K, both with the ionization degree $\eta \sim$ few per cent. The ‘high-temperature’ island has a minimum χ^2 larger than the ‘low-temperature’ solution by $\Delta\chi^2 \sim 6$. This difference while formally statistically significant is reduced when another background model is used. Long- and short-dashed lines show the relation between the temperature and the degree of ionization for CIE and radiatively cooling plasma (see Section 5.3), respectively.

$T = 10^2$ K and the ionization degree $\eta \equiv n_e/(n_e + n_H) = 0.025$ is marked with a black dot. As expected, there are two pronounced minima: at ~ 100 and $\sim 10^4$ K, both at $\eta \sim$ a few per cent. The corresponding spectra are shown in Fig. 12; they are further discussed in Section 5.3. In this analysis, the ‘high-temperature’ island has a χ^2 larger than the ‘low-temperature’ solution by $\Delta\chi^2 \sim 6$. Given the simplicity of the model, this difference is not sufficient to make a robust conclusion in favour of the low-temperature solution. We view both solutions as acceptable. The intermediate values can be reliably excluded. This non-monotonic behaviour over temperature arises because at temperatures in the range of 1000–7000 K, (i) the typical energy of a thermalized positron is below the 6.8-eV threshold of positronium formation via charge exchange with a hydrogen atom and (ii) radiative recombination with free electrons is suppressed relative to the direct annihilation with bound electrons.⁷ As a result, the positronium fraction is small at intermediate temperatures.

Overall, the results of this analysis and the implications for the properties of the ISM broadly agree with previous analyses of SPI data (Churazov et al. 2005; Jean et al. 2006) and earlier analyses by Bussard et al. (1979) and Guessoum et al. (1991).

5.3 Annihilation in a cooling ISM

The model spectra used in the previous section were calculated assuming that the temperature and the degree of ionization of the ISM do not change on the time-scales of positron slow-down and annihilation. This is not an obvious assumption since the time-scale for the annihilation of thermalized positrons can be longer than the ISM radiative cooling time-scale, as shown in Fig. 13. We define an isobaric cooling time-scale (black line in Fig. 13) as the ratio of the gas enthalpy to the radiative losses:

$$t_{\text{cool}} = \frac{\gamma}{\gamma - 1} \frac{nkT}{n^2\Lambda(T)}, \quad (5)$$

where $\gamma = 5/3$ is the gas adiabatic index, n the total gas density, k the Boltzmann constant, T the gas temperature and $\Lambda(T)$ the appropriately normalized cooling function, adopted from Sutherland & Dopita (1993). The slow-down time estimated for 500-keV positrons is shown with the blue line; for this estimate, we considered only Coulomb and hydrogen ionization losses (ignoring excitation losses and the contribution of helium). The temperature dependence of the slow-down time-scale in Fig. 13 arises due to the variations of the degree of ionization with temperature. For this plot, we adopted the collisional ionization equilibrium (CIE) from Arnaud & Rothenflug (1985). Finally, the red line shows the time-scale for annihilation of thermalized positrons, which includes

⁷ For an ionization degree of a few per cent.

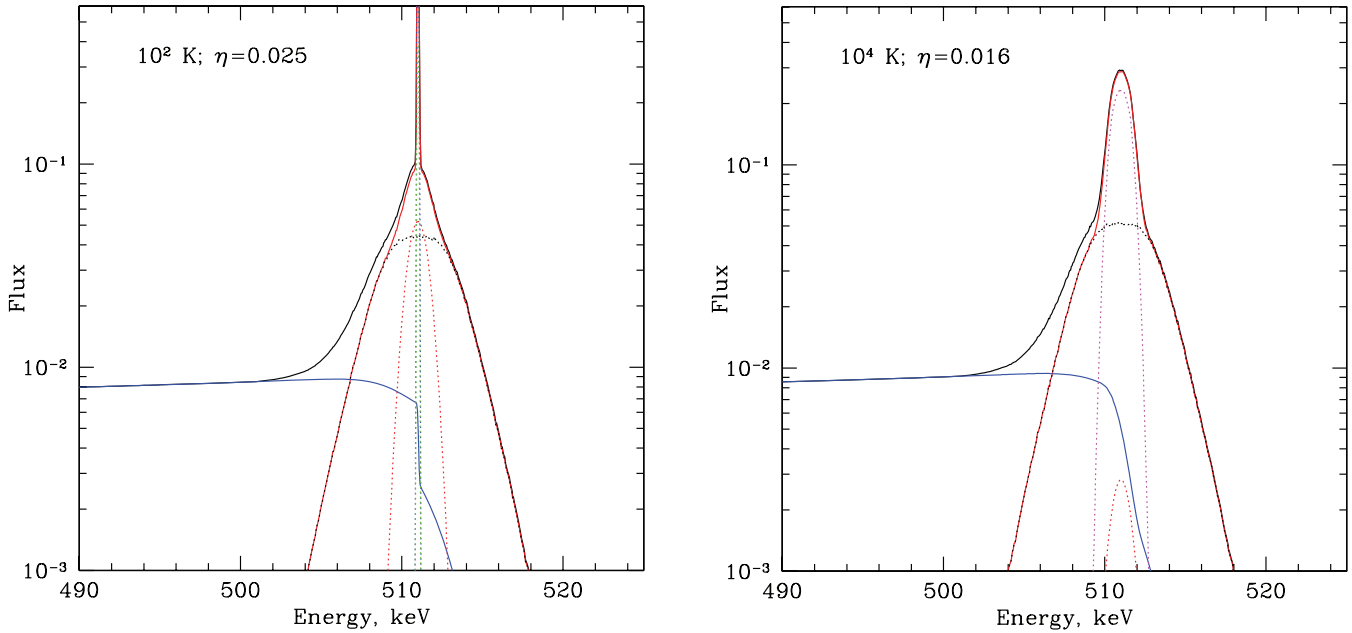


Figure 12. Left: expected annihilation spectrum for a 500-keV positron in a 100-K plasma with the hydrogen degree of ionization of 0.025. Right: the same as in the left-hand panel, but for 10^4 -K plasma and $\eta = 0.016$. The lines show as follows: solid black line – total annihilation spectrum; solid red line – total line spectrum; solid blue line – ortho-positronium continuum; dotted black line – in-flight charge exchange; dotted red line – thermalized positron annihilation with bound electrons; dotted blue line – radiative recombination of thermalized positrons; dotted green line – direct annihilation; magenta – charge exchange for thermalized positrons.

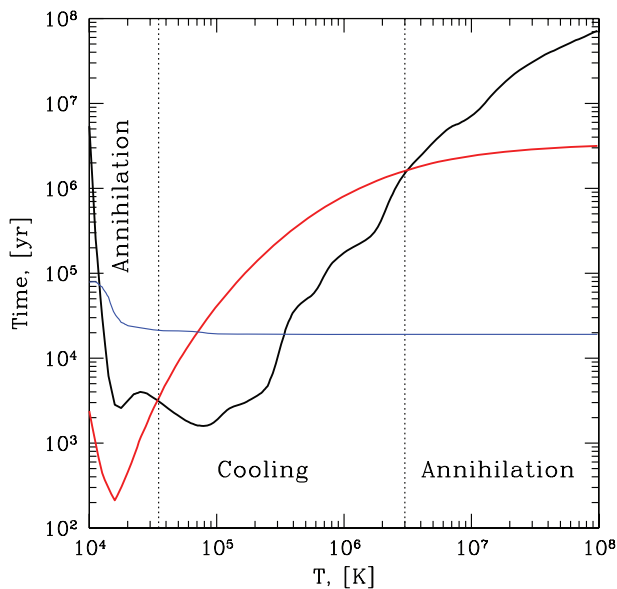


Figure 13. Comparison of different time-scales relevant for annihilation of positrons in a cooling ISM as a function of its temperature: cooling of gas (black), slowing down of positrons (blue) and annihilation of thermalized positrons (red). Calculations are done for the proton density of 1 cm^{-3} . The initial energy of positrons is assumed to be 500 keV. The dotted vertical lines separate the areas where cooling or annihilation dominates. For temperatures in the range from $\sim 3 \times 10^4$ to $\sim 3 \times 10^6$ K, the gas can cool faster than thermalized positrons annihilate. For instance, if 500-keV positrons are born in an $\sim 10^6$ -K ISM, the gas will cool down to a few 10^4 K before the positrons have a chance to annihilate. Once the temperature has dropped, the thermalized positrons will annihilate and the observer will see a gamma-ray spectrum indicating annihilation in an $\sim 10^4$ -K gas, regardless of the initial ISM temperature.

direct annihilation with free and bound electrons, charge exchange with hydrogen and radiative recombination.

From Fig. 13 it is clear that for temperatures in the range from $\sim 3 \times 10^4$ to $\sim 3 \times 10^6$ K, the gas is able to cool faster than thermalized positrons can annihilate. For temperatures outside this range, the annihilation time is shorter than the cooling time and the medium can to a first approximation be regarded as static. The most interesting conclusion that can be drawn from the comparison of time-scales in Fig. 13 is that if ~ 500 -keV positrons are born in an $\sim 10^6$ -K ISM, then the gas temperature will drop⁸ to a few 10^4 K before the positrons have a chance to annihilate. Once the ISM has cooled down, the positrons will annihilate and the observer will measure spectral characteristics typical of annihilation in warm gas, with no indication that the positrons were born in a hot medium.

We now proceed with calculating spectra expected for annihilation of positrons in a cooling ISM. This implies solving a time-dependent problem: for given initial gas temperature T_0 and kinetic energy of positrons E_0 , find the annihilation spectrum emitted while the gas cools down to a given final temperature T_1 . We solve this problem using a modified version of our Monte Carlo code, which retains from the original version the algorithms for the description of slowing down, thermalization and annihilation of positrons (in a pure hydrogen plasma).

The outcome of this calculation crucially depends on the assumptions made about the ionization state of the ISM during its cooling from $\gtrsim 10^6$ to $\lesssim 10^4$ K. In real astrophysical situations, a radiatively cooling plasma is expected to be substantially overionized relative to CIE, since the characteristic cooling time is shorter than the time-scale of hydrogen recombination. This will influence both the ISM cooling rate and the fate of positrons. We therefore adopt the temperature dependencies for the non-equilibrium ionization state

⁸ In the absence of an external source of heat.

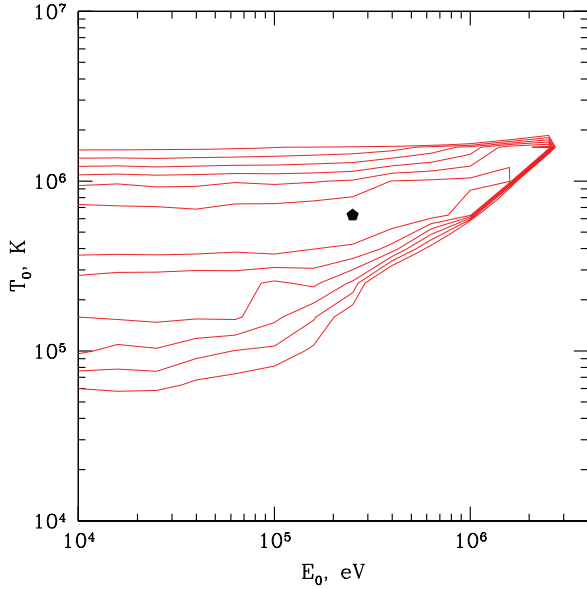


Figure 14. Contours of χ^2 for a grid of models for a cooling ISM over the range of initial ISM temperatures T_0 and initial positron energy E_0 . The minimum of $\chi^2 = 400.8$ achieved at $T_0 = 6.3 \times 10^5$ K and $E_0 = 250$ keV is marked with a black dot. Contours are plotted with an increment $\Delta\chi^2 = 3$.

and cooling rate of an isochorically cooling gas from Schmutzler & Tscharnuter (1993) and Gnat & Sternberg (2007), which cover the temperature range from 10^3 to 10^9 K (we assume that hydrogen is fully ionized at $T > 5 \times 10^6$ K). The temperature dependencies of the hydrogen ionization fraction for the CIE and non-CIE cases are compared in the right-hand panel of Fig. 11.

We carried out simulations covering a broad range of parameter values: $E_0 = 10$ keV–10 MeV, $T_0 = 10^4$ – 10^7 K. A run was terminated when the ISM cooled down to 10^3 K; it turns out that the absolute majority of positrons annihilate before the gas reaches this temperature, except for extreme values of the initial ISM temperature and positron energy. Although we assumed isochoric cooling, this assumption is not crucial, since the case of isobaric cooling is characterized by a very similar ISM ionization state and cooling rate (Schmutzler & Tscharnuter 1993).

Similar to the case of annihilation in a static medium considered in the previous section, we fit the spectra predicted by our cooling ISM models to the spectrum measured by SPI. In Fig. 14, we show contours of χ^2 values on the (E_0, T_0) plane. The best-fitting parameters are $E_0 \sim 250$ keV and $T_0 \sim 6 \times 10^5$ K (see the corresponding model spectrum and its fit to the SPI data in Fig. 15), with a large associated uncertainty region: the initial gas temperature and positron energy are allowed to take values from $\sim 2 \times 10^5$ to $\sim 10^6$ K and from 10 keV (the lower boundary of our simulations) to ~ 2 MeV, respectively. Therefore, the predicted gamma-ray spectrum is fairly insensitive to the initial parameters of the ISM and positrons. The reason for this is that in a broad range of E_0 and T_0 values, the main contribution to the total spectrum is provided by annihilations of thermalized positrons during the gas cooling from $\sim 10^5$ to $\sim 10^4$ K (when the positron annihilation time is a few times the ISM cooling time; see Fig. 13).

Judging by the small differences between the minimum χ^2 values, summarized in Table 4 (and recalling again that there are non-negligible systematic uncertainties associated with the data analysis), our best-fitting static ISM and cooling ISM models describe the SPI spectrum nearly equally well. In other words, we cannot strongly favour any of these models based on the available spectral data. In reality, this is mostly owing to the finite energy resolution of SPI. This becomes clear if we compare

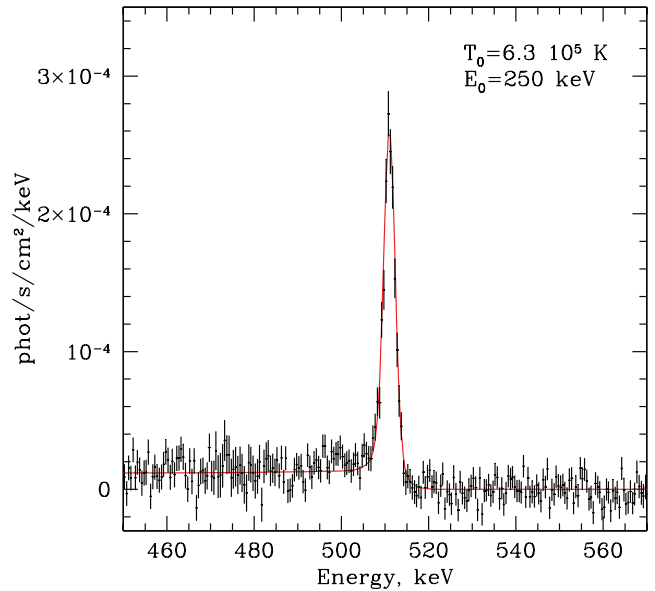
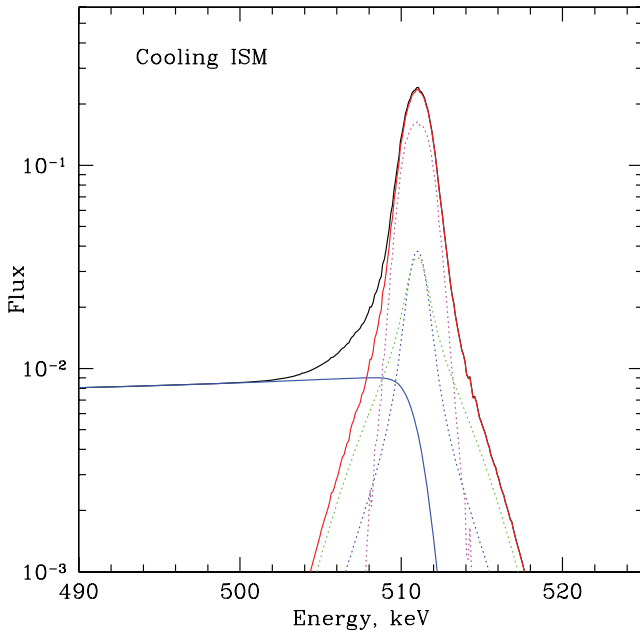


Figure 15. Left: expected annihilation spectrum for a radiatively cooling plasma with initial temperature $T_0 = 6.3 \times 10^5$ K and initial positron kinetic energy $E_0 = 250$ keV. Different lines show different spectral components, as in Fig. 12. In contrast to the annihilation in a static medium, the in-flight component makes negligible contribution for the cooling ISM solution, in which case the annihilation spectrum is essentially a superposition of spectra generated by thermalized positrons in gases with temperatures ranging from $\sim 10^4$ to $\sim 2 \times 10^5$ K. Right: spectrum of the annihilation radiation for a cooling ISM with initial temperature $T_0 = 6.3 \times 10^5$ K and initial positron energy $E_0 = 250$ keV in comparison with the observed bulge component spectrum in the bulge + disc model.

Table 4. Values of χ^2 for various spectral models for the bulge component spectrum in the 400–600 keV band (400 channels, 0.5 keV wide).

Model	Parameters	χ^2
Static ISM	$T = 10^2$ K; $\eta = 0.025$	402.4
Static ISM	$T = 10^4$ K; $\eta = 0.016$	408.6
Cooling ISM	$T_0 = 6.3 \times 10^5$ K; $E_0 = 250$ keV	400.8

the spectra predicted by the different models, shown in Figs 12 and 15.

6 DISCUSSION

A comprehensive answer to the fundamental question of the origin of the bulk of annihilating positrons should explain a number of key observational facts, including the total production rate of positrons ($\sim 10^{43}$ positrons per second within the Galactic bulge), the dominance of the bulge compared to the disc, the morphology of the 511-keV line emission (a $8^\circ \times 6^\circ$ ‘bulge’ plus a more extended, along the Galactic plane, ‘disc’ component) and the spectral properties of the bulge component, which (within the accuracy allowed by the SPI energy resolution) resemble the annihilation of positrons in a warm ($\sim 10^4$ K) or cold ($\sim 10^2$ K) medium with the ionization degree of a few per cent.

On these grounds (flux and morphology), such a straightforward explanation as ^{26}Al or the interaction of cosmic rays with the ISM is disfavoured. The morphology problem can be partly alleviated by assuming transport of the positrons away from the place where they are born (e.g. Prantzos 2006). Recently, an attempt to provide a self-consistent model was done by Higdon et al. (2009) and Lingenfelter et al. (2009). Their model assumes that supernovae are the source of positrons (via β^+ decay of ^{56}Ni , ^{44}Ti and ^{26}Al) in the Galaxy and the propagation of positrons in the ISM is different in the bulge and in the disc. The difference in propagation explains the weakness of the disc compared to the bulge – a large fraction of positrons born in the disc escape into the halo, while only a small fraction of positrons escape the bulge. In the bulge, the positrons diffuse through the ISM and annihilate when entering the H II and H I envelopes of molecular clouds – this explains the spectral properties of the annihilation emission. Finally, the morphology of the bulge is explained by annihilation in a tilted disc within 1.5 kpc of the GC. The key assumptions in the Higdon et al. model are that (i) magnetic flux tubes are almost radial in the bulge region and (ii) propagation of positrons along the flux tubes can be treated in the diffusion approximation with the frequency of scattering (or the mean free path) estimated from scaling the energy density of magnetic fields down to the Larmor radius. Their estimate of the mean free path in the bulge region is large enough to allow positrons to reach the tilted disc (see Section 3.4) before they slow down and annihilate. Thus, the morphology of the tilted disc gives the source of annihilation radiation in the GC its characteristic shape.

Here we consider the alternative possibility that the thermal evolution of the ISM plays the key role in the GC annihilation emission. The key assumption of the model is that the medium in which the bulk of positrons is produced and annihilates has a cooling time shorter than the slow-down and annihilation time-scales. From Fig. 13, it follows that the temperature ought to be lower than $\sim 3 \times 10^6$ K.

Gas with temperature in the range of 10^5 –few 10^6 K is observed in the Galaxy, as indicated by e.g. C VI, O VII and O VIII lines (e.g.

McCammon et al. 2002). An ISM with a temperature of $\sim 3 \times 10^6$ K is also observed in the central region of M31 (Bogdán & Gilfanov 2008). The origin of this gas is not clear. For a long time, observations of 6.7- and 6.9-keV lines of heavily ionized iron and an unresolved X-ray glow (at energies above a few keV) of the Galactic plane were regarded as evidence for a much hotter, $\sim 10^8$ -K, plasma filling most of the bulge’s volume (e.g. Koyama et al. 1986). Positrons injected into such a medium will slow down and annihilate before the plasma is able to cool (Fig. 13), and a very broad annihilation line without an ortho-positronium continuum is expected to be observed, in stark contrast with observations. However, recent observations (Revnivtsev et al. 2006, 2009; Sazonov et al. 2006) have convincingly demonstrated that the apparently diffuse Galactic X-ray emission is in fact a superposition of millions of faint compact sources – accreting white dwarfs and coronally active stars. This removes the problem of confining $\sim 10^8$ -K gas by the gravitational well of the Galaxy. Cooler, 10^5 –few 10^6 K, gas can on the contrary be trapped in the Galaxy potential. For instance, the density of 2×10^6 K gas in hydrostatic equilibrium in the Milky Way potential would drop by a factor of $\sim 3 \times 10^3$ at a distance of ~ 1.5 kpc above the plane. This means that such gas can accumulate in the Galactic bulge.

However, a self-consistent model explaining the few 10^6 -K ISM in the bulge of the Milky Way or in M31 is still missing. If one takes the mass loss rate by evolving stars (e.g. Ciotti et al. 1991) and the total energy and iron input rate from SNIa (e.g. Mannucci et al. 2008), then a ‘natural’ temperature of the gas is of the order of a few keV (mean energy per injected particle) and the expected abundance of iron is about five times the solar value. These parameters do not fit the properties of the observed few 10^6 -K component of the ISM. Tang et al. (2009) and Tang & Wang (2010) argue that the account for non-uniformity and intermittence in energy injection by SNIa leads to a broad gas distribution over temperature with a lower than the mean temperature component making the largest contribution to the observed X-ray emission. It is not yet clear if this provides a full explanation of the origin of 10^6 -K gas. We therefore make an ad hoc assumption that a few million degree medium is widespread in the Milky Way bulge.

The positron annihilation in a cooling ISM (Section 5.3) can resolve some of the issues mentioned at the beginning of this section. Indeed, if the ISM is able to cool down to 10^5 – 10^4 K before the positrons annihilate, then the observer will always see a spectrum characteristic of annihilation in a warm plasma. This resolves the question of why positrons are apparently annihilating in a warm/cold medium even though such a medium should have a relatively small filling factor. Otherwise, the positrons would have to be produced preferentially in the warm and/or cold ISM phases or to migrate between phases. In the cooling ISM model, this is not required. If the ISM is dynamic and goes through cooling/heating cycles, then even those positrons born in the hot phase will annihilate in a warm (10^4 – 10^5 K) gas. Transport of positrons over large distances is not required in this model. Some moderate transport of positrons will not contradict the model, since it will just make shorter the lifetimes of positrons initially born in the hot ISM, but the positrons will still predominantly annihilate while migrating through the warm/cold ISM phases.

Putting all arguments together, it seems plausible that the following model might work.

(i) Positrons are injected in volume-weighted fashion into the ISM (e.g. by SNIa). This means that most of the positrons are initially in the hot ISM phase. The key requirement of the model is

that the large volume fraction has to be occupied by a few 10^6 -K gas, which may not be true in the Galactic bulge.

(ii) The plasma cools radiatively before the positrons slow down. An outflow, adiabatic expansion of the gas advect/move positrons and may contribute to positron cooling.

(iii) Eventually, the plasma reaches relatively low temperatures and the positrons annihilate, producing the spectral features as observed by SPI.

If correct, this model predicts that there should be some similarity in the spatial distribution of the annihilation emission and the thermal emission of plasma with temperature in the 10^4 – 2×10^5 K range. Outflows from the central regions of normal galaxies are well known. A good example is M31 with clear evidence of hot $\sim 3 \times 10^6$ K gas (Bogdán & Gilfanov 2008), possibly outflowing from the central region. In subsequent publications, we plan to consider the dynamics of galactic outflows, advection and annihilation of positrons and the expected spectral signatures (in soft X-ray and other wavebands) of the main annihilation sites.

7 CONCLUSIONS

We have analysed SPI/INTEGRAL data on the 511-keV line from the GC, accumulated over ~ 6 yr of observations.

Using a simple two-component bulge + disc model, we have constructed the broad-band energy spectra of both components. The bulge component shows a prominent 511-keV line and essentially no flux at 1.8 MeV, while the disc component on the contrary contains a prominent 1.8-MeV line and a very weak annihilation line. The inferred annihilation rate in the bulge component is $\sim 10^{43}$ positrons per second (for $f_{\text{ps}} = 1$).

The FWHM of 511 keV in the bulge is 2.40 ± 0.16 keV. The flux ratio of the line to three-photon continuum corresponds to a fraction of positrons annihilating via positronium formation close to unity ($f_{\text{ps}} = 1.00 \pm 0.02$). Our experiments with using slightly different SPI background models have yielded f_{ps} in the range of 0.96–1. This combination of spectral parameters can be explained in terms of a single-phase static ISM model as annihilation of positrons in a warm ($\sim 10^4$ K) or cold ($\sim 10^2$ K) medium with the hydrogen ionization fraction of a few per cent.

We have demonstrated that the observed annihilation spectrum of the bulge component can also be explained with a model of positrons annihilating in a radiatively cooling ISM, provided that the initial temperature of the ISM is in the range of 2×10^5 – 10^6 K. In such a medium, the ISM cools down to $\sim 10^5$ – 10^4 K before the positrons are able to annihilate and the observer sees an annihilation spectrum typical of a warm ISM. This suggests that the positrons might be initially injected into the hot ISM phase, which has the largest filling factor in the Galaxy, but the annihilation occurs only when the gas has cooled down to a relatively low temperature, effectively erasing the memory on the initial conditions (the initial temperature and ionization state of the ISM and the initial energy of positrons). If there is an outflow of hot gas, then the positrons will be advected with the flow and annihilate in the part of the flow where the temperature has dropped to 10^5 – 10^4 K. The mass of the cooling gas need not be large – it is enough to assume that the initially hot ISM phase occupies the largest fraction of the volume where the positrons are produced, provided that positrons do not migrate freely between phases. The key requirement of the model is that the large fraction of the bulge's volume is occupied by a few 10^6 -K gas. In this paper, this is adopted as an ad hoc assumption. The origin of this gas is not entirely clear, although observations

suggest that this component is present in the central part of the Galaxy.

ACKNOWLEDGMENTS

We are grateful to Roland Diehl, Umberto Maio, Sergey Molkov and Jean-Pierre Roques for useful discussions. This work was supported by the DFG grant CH389/3-2, grant NSH-5069.2010.2, programmes P-19 and OFN-16 of the Russian Academy of Sciences and the RFBR grant 09-02-00867. SS acknowledges the support of the Dynasty Foundation.

REFERENCES

- Aharonian F. A., Atoyan A. M., 1981a, *Soviet Astron. Lett.*, 7, 395
 Aharonian F. A., Atoyan A. M., 1981b, *Phys. Lett. B*, 99, 301
 Aharonian F. A., Atoyan A. M., 2000, *A&A*, 362, 937
 Arnaud M., Rothenflug R., 1985, *A&AS*, 60, 425
 Beacom J. F., Bell N. F., Bertone G., 2005, *Phys. Rev. Lett.*, 94, 171301
 Bogdán A., Gilfanov M., 2008, *MNRAS*, 388, 56
 Bouchet L., Jourdain E., Roques J.-P., Strong A., Diehl R., Lebrun F., Terrier R., 2008, *ApJ*, 679, 1315
 Bussard R. W., Ramaty R., Drachman R. J., 1979, *ApJ*, 228, 928
 Churazov E., Gilfanov M., Forman W., Jones C., 1996, *ApJ*, 471, 673
 Churazov E., Sunyaev R., Sazonov S., Revnivtsev M., Varshalovich D., 2005, *MNRAS*, 357, 1377
 Ciotti L., D'Ercole A., Pellegrini S., Renzini A., 1991, *ApJ*, 376, 380
 Diehl R., Lang M., Kretschmer K., Wang W., 2008, *New Astron. Rev.*, 52, 440
 Ferrière K., Gillard W., Jean P., 2007, *A&A*, 467, 611
 Gehrels N., Barthelmy S. D., Teegarden B. J., Tueller J., Leventhal M., MacCallum C. J., 1991, *ApJ*, 375, L13
 Gnat O., Sternberg A., 2007, *ApJS*, 168, 213
 Guessoum N., Ramaty R., Lingenfelter R. E., 1991, *ApJ*, 378, 170
 Guessoum N., Jean P., Gillard W., 2005, *A&A*, 436, 171
 Higdon J. C., Lingenfelter R. E., Rothschild R. E., 2009, *ApJ*, 698, 350
 Jean P. et al., 2003, *A&A*, 407, L55
 Jean P., Knödseder J., Gillard W., Guessoum N., Ferrière K., Marcowith A., Lonjou V., Roques J. P., 2006, *A&A*, 445, 579
 Johnson W. N., Haymes R. C., 1973, *ApJ*, 184, 103
 Johnson W. N., Harnden F. R., Haymes R. C., 1972, *ApJ*, 172, L1
 Knödseder J. et al., 2005, *A&A*, 441, 513
 Koyama K., Makishima K., Tanaka Y., Tsunemi H., 1986, *PASJ*, 38, 121
 Leventhal M., MacCallum C. J., Stang P. D., 1978, *ApJ*, 225, L11
 Lingenfelter R. E., Higdon J. C., Rothschild R. E., 2009, *Phys. Rev. Lett.*, 103, 031301
 Liszt H. S., Burton W. B., 1980, *ApJ*, 236, 779
 Liszt H. S., Burton W. B., 1996, in Blitz L., Teuben P., eds, *Proc. IAU Symp.* 169. *Motions and Deformations of the Inner-Galaxy Neutral Gas Layer*. Kluwer, Dordrecht, p. 297
 López-Corredoira M., Cabrera-Lavers A., Gerhard O. E., 2005, *A&A*, 439, 107
 McCammon D. et al., 2002, *ApJ*, 576, 188
 Mahoney W. A., Ling J. C., Wheaton W. A., 1994, *ApJS*, 92, 387
 Mannucci F., Maoz D., Sharon K., Botticella M. T., Della Valle M., Gal-Yam A., Panagia N., 2008, *MNRAS*, 383, 1121
 Ore A., Powell J. L., 1949, *Phys. Rev.*, 75, 1696
 Plüschke S. et al., 2001, in Battick B., ed., *ESA SP Conf. Vol. 459, Exploring the Gamma-Ray Universe*. ESA-SP, Noordwijk, p. 55
 Prantzos N., 2006, *A&A*, 449, 869
 Purcell W. R. et al., 1997, *ApJ*, 491, 725
 Revnivtsev M., Sazonov S., Gilfanov M., Churazov E., Sunyaev R., 2006, *A&A*, 452, 169
 Revnivtsev M., Sazonov S., Churazov E., Forman W., Vikhlinin A., Sunyaev R., 2009, *Nat*, 458, 1142

- Roques J. P. et al., 2003, *A&A*, 411, L91
Sazonov S., Revnivtsev M., Gilfanov M., Churazov E., Sunyaev R., 2006, *A&A*, 450, 117
Schmutzler T., Tscharnuter W. M., 1993, *A&A*, 273, 318
Sizun P., Cassé M., Schanne S., 2006, *Phys. Rev. D*, 74, 063514
Sturmer S. J. et al., 2003, *A&A*, 411, L81
Sutherland R. S., Dopita M. A., 1993, *ApJS*, 88, 253
Tang S., Wang Q. D., 2010, *MNRAS*, 408, 1011
Tang S., Wang Q. D., Mac Low M.-M., Joung M. R., 2009, *MNRAS*, 398, 1468
Teegarden B. J. et al., 1996, *ApJ*, 463, L75
Teegarden B. J. et al., 2005, *ApJ*, 621, 296
Tsygankov S., Churazov E., 2010, *Astron. Lett.*, 36, 237
Vedrenne G. et al., 2003, *A&A*, 411, L63
Wang W. et al., 2009, *A&A*, 496, 713
Weidenspointner G. et al., 2003, *A&A*, 411, L113
Weidenspointner G. et al., 2008, *Nat*, 451, 159
Winkler C. et al., 2003, *A&A*, 411, L1

This paper has been typeset from a \TeX/L\AA\TeX file prepared by the author.